The radio galaxy Pictor A – a study with the VLA

Richard A. Perley[1]**, Hermann-Josef Röser**[2]**, and Klaus Meisenheimer**[2]

[1] National Radio Astronomy Observatory[*], Socorro, NM 87801, USA
[2] Max-Planck-Institut für Astronomie, Königstuhl 17, D-69117 Heidelberg, Germany

Abstract. Detailed multi-frequency VLA observations of the prominent southern radio galaxy Pictor A are described. The radio structure is found to comprise very dim, nearly circular lobes with an extraordinarily bright and compact hot spot located at the western extremity of the western lobe. A faint jet is observed to connect this hot spot with the radio nucleus. No counter-jet is seen. The eastern lobe contains two hot spots of much lesser brightness and compactness. The radio lobes have significantly different spectral indices, with the eastern (un-jetted) lobe being 'steeper'. Enhanced spectral steepening is found in the central regions surrounding the radio nucleus, and around the peripheries of both radio lobes. The eastern lobe depolarizes at a higher frequency than the western lobe, and also displays a much higher rms scatter in the derived rotation measure, although the mean rotation measure is very similar in both lobes. Steepening of the high frequency spectral index ($\lambda 6\,\mathrm{cm}$ to $\lambda 2\,\mathrm{cm}$) is seen in the lobe near to the western hot spot.

From the similarity in the structure of the western hot spot – including the extended filament – between radio and optical wavelength ranges it is concluded that all of the extended optical emission is due to the synchrotron process. The implications of these findings are discussed.

Key words: Acceleration of particles – polarization – radiation mechnisms: non-thermal – galaxies: Pictor A – radio continuum: galaxies

1. Introduction

The radio galaxy Pictor A is one of the most prominent but least studied objects in the radio sky, appearing 6th in the 408 MHz all-sky survey of Robertson (1973) of extragalactic radio sources. Unfortunately, its declination of $-46°$ makes imaging by northern hemisphere instruments difficult or impossible, with the re-

sult that the best images are of low resolution. Consequently, little is known of the detailed radio properties of this object.

Our interest in Pictor A is due to the discovery by Röser and Meisenheimer (1987) of bright, compact, highly polarized optical emission from a region close to, or identical with, the western hot spot shown in the best available radio image. The optical emission from this region is extraordinary, for it comprises a highly polarized, unresolved knot with $m_B = 19.5^{\mathrm{mag}}$, exhibiting a featureless spectrum, and an associated filament of several kiloparsecs extent separated from the bright knot by several kiloparsecs. Röser and Meisenheimer, on the basis of the spectrum and polarization, concluded that the optical knot emission is due to the synchrotron process, and thus very likely represents the site of local particle acceleration. However, the extended emission was too faint to allow measurement of the spectrum or polarization, so the emission mechanism of this region remains unknown. If synchrotron radiation, this extension would be difficult to understand within the framework of current models, as the lifetimes of optical synchrotron emitting electrons are too short to allow them to migrate from the current hot spot to the filament, or to have been left behind by the hot spot as it passed through the area towards its present position.

Although the presence of optical emission near the prominent western radio hot spot was our original motivation to observe Pictor A, the object is an excellent candidate for a comprehensive study of the radio emission of an active galaxy, for it is a large, luminous and nearby radio source – characteristics which enable Pictor A to be mapped with excellent linear resolution and signal-to-noise ratio. Further, the extraordinary brightness ratio between the western hot spot and the unusually dim and circular lobes argues for some unusual differences between this object and more 'normal' examples of radio-loud AGN. Detailed observations of this source should help our general understanding of the physics governing the formation and evolution of radio-loud galaxies and quasars. We thus embarked on a comprehensive observing programme of this object with the Very Large Array.

This paper describes in detail the results of our radio observational study of Pictor A, which encompassed all available observing bands and configurations of the Very Large Array.
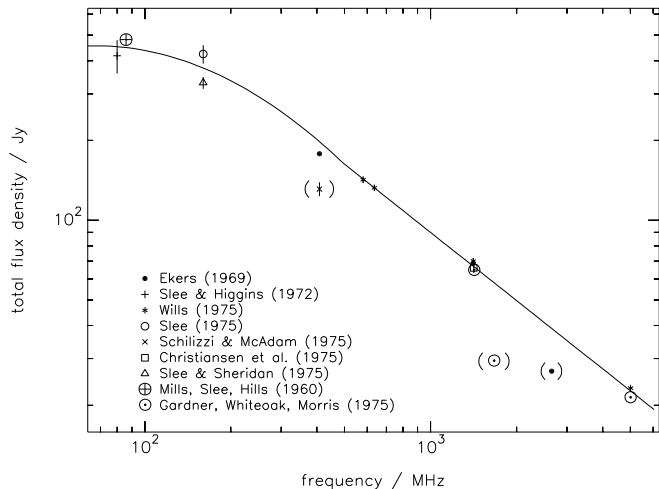
Fig. 1. The radio spectrum of Pictor A, taken from the published literature. As there is evidence for curvature at lower frequencies we fitted a straight line of index $\alpha = 0.85$ for $\nu > 400$ MHz only. The points plotted within brackets mark those we believe affected by resolution.

Sect. 2 gives a detailed history of studies of Pictor A. In Sect. 3 we discuss our VLA observations, and in Sect. 4, the new radio images of the source and its hot spots are shown. Sec. 5 contains a discussion of issues raised by these new observations.

2. Past observations of Pictor A

2.1. Flux density and spectrum

Pictor A is a prominent radio source, having been discovered and named by Stanley and Slee (1950). Although the reality of this discovery was doubted at first, subsequent surveys with better instruments confirmed its existence (Mills (1952), Bolton, Stanley and Slee (1954), Mills et al. (1960)). In the all-sky listing of Robertson (1973), Pictor A is listed as the 6th strongest[1] extragalactic radio source, although this standing should be incremented by one since Cygnus A is omitted from the survey. The integrated spectrum of Pictor A is shown in Fig. 1. The plotted points have been taken from the literature, and have been corrected to the scale of Baars et al. (1977) using the factors given in that paper. The spectrum is well fitted by a power-law spectrum of slope $\alpha = 0.85$[2] between the frequencies of 400 and 5000 MHz. There is evidence of a flattening of the spectrum below 400 MHz, although it is difficult to assess the degree of the flattening since the measured values are in considerable disagreement. Our fitted spectrum has used the results of Wills (1975) with high weight, since it is clear that she has been most careful in the calibration of the data, accounting for the various sources of error, and in the accounting for the resolution of Pictor A.

---

[1] 'Strongest' here means as ranked by observed spectral flux density, and is not to be confused with either luminosity or intensity.
[2]   The spectral index α is defined by $S_\nu \propto \nu^{-\alpha}$.

Slee and Sheridan (1975) noted that the spectra of the two lobes were slightly different. The flux density ratio of the East and West lobes varies from 1.2 at 80 MHz (Morimoto and Lockhart, 1968) to 1.12 at 160 MHz (Slee and Sheridan, 1975), 1.02 at 408 MHz (Schilizzi and McAdam, 1975) and 0.91 at 5000 MHz (Wills, 1975). It thus appears that the eastern lobe has a steeper spectrum than the western.

The spectral luminosity of Pictor A at 1465 MHz is $7.4/h^2 \times 10^{25}$ erg s^{-1}, placing this object well within the luminosity range of FR II radio sources (Fanaroff and Riley, 1974).

2.2. Basic structure

Hints of the significant angular size of Pictor A date back to work by Bolton et al. (1954). Maltby and Moffet (1962) were the first to report the basic double structure, tentatively describing the source as being comprised of two equal components of size $2'$, separated by $4.'6$ along position angle p.a. $= 90°$. They noted, however, that the structure was probably too complex to be described as a simple, two-component double. Broten et al. (1965) clearly resolved the source into a nearly equal double along p.a. $= 110°$. Ekers (1967), (1969), using a non-phase-stable variable spacing interferometer with a maximum baseline of 1950λ, proposed a four-component model: Two equal components of size $3.'0 \times 1.'5$ along p.a. $= 105°$ separated by $4.'1$ along the same p.a. , plus two components of size $< 0.'5$ separated by $6.'9$ along the same p.a. . This combination of a pair of extended components with a pair of compact components located near the outer extremities describes what is now known as a FR II radio source. Schwarz, Whiteoak and Cole (1971), using the same instrument, but in a phase-stable mode, produced an image clearly showing the hot spots located at the extremities of the lobes, with the western hot spot much brighter than the eastern one. Finally, the Fleurs Synthesis Telescope (FST), a newer instrument with greatly improved (u, v) coverage and a resolution of $45''$, was used by Christiansen et al. (1977) to produce the best radio image of Pictor A available until the advent of the VLA. The latter was used by Prestage (1985) in a 'quick-look' mode, and resolved the eastern hot spot into two components.

2.3. Radio nucleus

The earliest estimates of the radio flux density from the nucleus of Pictor A were provided by the techniques of VLBI. Schilizzi (1976) gave the flux density as 0.9 Jy at 8.1 GHz, while Christiansen et al. (1977) quote Fomalont, who used the Green Bank 35 km-interferometer, as assigning ~ 0.5 Jy to the nucleus at both 2.7 and 8.1 GHz. The same authors, using their FST data at 1400 MHz, estimate 0.5 Jy at 1.4 GHz. Prestage (1985) using the VLA, found 0.85 Jy at 5.0 GHz, and 1.25 Jy at 1.4 GHz. Considering the diverse origins of these estimate, and the likelihood of time-variability, we can conclude only that Pictor A has a flat-spectrum core – with a flux of roughly 5 % of the total source flux density rather strong for a radio galaxy.

2.4. Radio polarimetry

The radio polarization of Pictor A was studied by Seielstad (1967), and Seielstad and Weiler (1969), using the Owens Valley Radio Observatory two-element interferometer, and by Davies and Gardner (1970), Gardner and Whiteoak (1971), Gardner, Whiteoak and Morris (1975), using the Parkes 64-meter antenna. Further polarimetry was attempted by Schwarz, Whiteoak and Cole (1971), using the Parkes interferometer. In general, these studies showed that Pictor A appeared to have very low polarization (generally less than 5%). Most of these papers pointed out that a strong polarization maximum was located at the western end of the source, corresponding to the western hot spot.

Although the polarized flux on the arc minute scale was rather low, there was sufficient signal to determine the rotation measure (RM) of the source. Haves (1975) found $RM = (51 \pm 4)\,\mathrm{rad\,m^{-2}}$, based on data of his own and from the literature. Seielstad and Weiler (1969), found $50\,\mathrm{rad\,m^{-2}}$, while Berge and Seielstad (1967) obtained $46\,\mathrm{rad\,m^{-2}}$. Gardner and Whiteoak (1971) found little evidence for a rotation measure gradient across the source, contradicting a result of Seielstad and Weiler (1969).

2.5. Optical and X-ray observations

Pictor A was identified with a 19^{mag} galaxy by Bolton, Gardner, and Mackey (Bolton et al., 1964), on the basis of an improved position from the Parkes 64m-radio-telescope. Schmidt (1965), using the $200''$-telescope, determined the redshift to be $z = 0.0342$ on the basis of a rich emission line spectrum[3]. Schmidt also estimated the magnitude to be $m_V = 16^{\mathrm{mag}}$. Three-color photometry by Westerlund and Wall (1969) found $m_V = 15.77^{\mathrm{mag}}$, with normal colors for a radio galaxy. They describe the galaxy as an N-galaxy, although others have classified it as an E-galaxy. Danziger, Fosbury and Penston (1974) took direct photographs of the galaxy as well as spectrophotometric scans. They find the presence of a relatively sharp nucleus, but otherwise no spiral or filamentary structure. The spectrum shows lines originating from ions with a wide range of ionization potentials having very large widths.

In a survey for optical emission from radio hot spots Röser and Meisenheimer (1987) found a highly polarized compact object of 19.5^{mag} near the vicinity of the western hot spot of Pictor A. Due to the high linear polarization and featureless optical spectrum they identified the object with the radio hot spot. This counterpart was also marginally detected in the EINSTEIN data (Röser and Meisenheimer, 1987). Subsequently, ROSAT HRI data confirmed the existence of an X-ray source which coincides with the hot spot position, and which cannot be of synchrotron origin (Röser et al., in preparation).
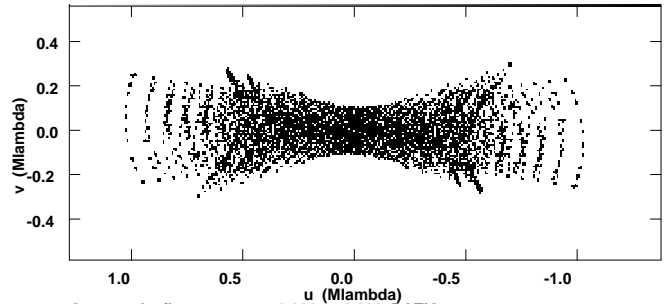
---

[3]   For $H_0 = 100\,h\,[\mathrm{km\,sec^{-1}\,Mpc^{-1}}]\,1''$ corresponds to $450/h$ pc.

Fig. 2. The distribution of measurements in the spatial frequency plane normal to the direction to the radio source (the u, v-plane). The distribution shown is taken from our $\lambda 3.6$ cm-observations taken in A-configuration.

3. VLA radio observations

Pictor A lies at a declination of $-45°.8$, making it a difficult object to observe from the northern hemisphere. At the latitude of the VLA the source never exceeds an elevation of $10°$, which when combined with the VLA's limiting elevation of $7°.5$, allows only 2.5 hours observing per day. Besides limiting sensitivity, this short observing period greatly restricts the (u, v)-coverage, which limits the dynamic range and fidelity of the derived images. In addition, the low elevation greatly enhances atmospheric corruption of the data, making accurate imaging very difficult unless self-calibration techniques are employed.

Table 1 contains a summary of all our successful observing runs, and shows that all the VLA's hybrid configurations were employed with three additional runs with the full A-configuration. Nevertheless, the resulting (u, v)-coverage is far from ideal. Fig. 2 shows a typical distribution of measured spacings. The 'bow-tie' distribution in the uv-plane, i.e. the lack of N-S resolution, especially along the v-axis, and the sharp corners, combined with the low density of measured values at large E-W spacings (along the u-axis) make reliable deconvolution difficult. We have adopted a conservative approach in deconvolution – for images of large-scale, low brightness distributions, we have 'circularized' the array by using a taper in the deconvolution algorithms so that only those measurements interior to a circle whose radius equals the maximum N-S spacing at $u = 0$ were utilized. This reduces the VLA's A-configuration to an effective configuration mid-way between B and C. For compact high brightness regions, the hot spots and nucleus, we have used all the data. In these cases the restoring beam is highly elliptical with an axial ratio of $\sim 5{:}1$.

We observed Pictor A at 4, P, L, C, X, and U bands ($\lambda\lambda 400$, 90, 20, 6, 3.6, and 2 cm respectively) according to the schedule shown in Tab. 1. Observations at K-band ($\lambda 1.3$ cm) in the A-configuration were attempted, but were not successful due to severe atmospheric phase gradients and insufficient sensitivity to allow self-calibration.

The VLA allows simultaneous observations of two different frequencies within the same band in both circular polarizations. The frequencies and bandwidths chosen are shown in the table.

Table 1. VLA-observations of Pictor A

Band λ [cm]	Frequency [MHz]	α (1950)	δ (1950)	Config.	Date	Duration [h]	BW [MHz]	Δt [sec]
4 400	73.8	$5^h\ 18^{min}\ 18\overset{s}{.}0$	$-45°\ 49'\ 39\overset{''}{.}0$	A	19 & 23/11/96	5.0	1.625	10
				A	4 & 23/01/97	2.0	1.625	10
				AnB	10/10/91	0.5	1.625	10
P 90	327.5 / 333.0	$5^h\ 18^{min}\ 18\overset{s}{.}0$	$-45°\ 49'\ 39\overset{''}{.}0$	A	3/10/87	0.2	3.125	6
				AnB	29/10/87	0.3	6.25	10
				AnB	10/10/91	0.5	3.125	10
				BnC	22/02/88	0.8	3.125	10
				CnD	24/06/88	0.8	3.125	30
L 20	1446 / 1496	$5^h\ 18^{min}\ 18\overset{s}{.}0$	$-45°\ 49'\ 39\overset{''}{.}0$	A	3/10/87	1.0	3.125	6
				A	1/10/87	0.1	12.5	10
				AnB	3/07/86	1.3	12.5	10
				BnC	2/10/86	1.3	12.5	20
				CnD	1/02/87	0.8	12.5	20
C 6	4822 / 4872	$5^h\ 18^{min}\ \ \ 9\overset{s}{.}0$	$-45°\ 49'\ 17\overset{''}{.}0$	A	3/10/87	0.9	6.25	6
				A	1/10/87	0.1	25.0	10
				AnB	3/07/86	1.2	25.0	10
				BnC	2/10/86	1.1	25.0	20
X 3.6	8415 / 8465	$5^h\ 18^{min}\ \ \ 0\overset{s}{.}09$	$-45°\ 48'\ 53\overset{''}{.}9$	A	12/03/90	0.7	50.0	3
				AnB	10/10/91	0.6	50.0	10
U 2	14915 / 14965	$5^h\ 18^{min}\ \ \ 0\overset{s}{.}09$	$-45°\ 48'\ 53\overset{''}{.}9$	A	2 & 7/03/90	1.7	50.0	3
				AnB	26 & 29/10/87	2.4	50.0	6
				BnC	2/10/86	1.2	50.0	20
				CnD	2 & 3/02/87	2.4	50.0	20

The bandwidths were chosen to minimize bandwidth broadening (equivalent to chromatic aberration) of the resulting image at all bands except at 4-band and P-band, where the narrow bandwidths chosen were dictated by the local RFI (radio frequency interference) environment. The phase center chosen varied with band since the angular size of the source is such that considerable attenuation of the structure occurs at U, X, and C bands. At X and U bands, only the region around the western hot spot could be imaged in a single field. Additional short observations of the nuclear regions at X-band were made in order to obtain an accurate position of the radio core, and to determine the existence of any radio jet. The table also shows the on-line integration time Δt. For the extended configurations, the rapid phase fluctuations forced the use of very short on-line integration times. After removal of these fluctuations by software, the data were averaged to much longer intervals (typically 30 seconds), to allow more efficient use of the imaging algorithms.

The data were initially calibrated through observations of $0537-441$, whose flux scale was set to the Baars et al. (1977) scale through observations of 3C 48 or 3C 286. Because of the extremely low elevation of Pictor A, the effects of opacity must be considered in bootstrapping the flux scale. The atmospheric opacity in the radio band is due to a band of spin-rotation oxygen lines near 60 GHz, plus a weak water vapor transition near 23.24 GHz. At wavelengths longer than $\lambda 3.6$ cm, the water vapor transition is unimportant, and the zenith opacity due to the far wings of the oxygen transitions is nearly constant at $\tau = 0.008$. At wavelengths shorter than $\lambda 6$ cm, the water vapor transition must be considered, resulting in a higher, and vari-

able opacity. We have taken the zenith opacity to be 0.011 and 0.0165 at $\lambda 3.6$ cm and $\lambda 2$ cm, respectively – values which are typical for VLA observing in clear weather. At the elevation of Pictor A, the attenuation is 4% at $\lambda 20$ cm, $\lambda 90$ cm, and $\lambda 6$ cm, 5% at $\lambda 3.6$ cm, and 9% at $\lambda 2$ cm.

To this must be added the dependence of the antenna gain on elevation. Recent tests demonstrate that the average power gain of the VLA antennas changes by less than 1% over the observable elevation range from ten to ninety degrees at wavelengths longer than $\lambda 2$ cm, and that the change of gain at $\lambda 2$ cm is about 5% between elevations of 50 and 10 degrees. Thus, the effective total reduction of flux density at $\lambda 2$ cm is expected to be $\sim 14\%$, and about 5% at all other bands used in these observations.

However, these effects were not understood by us at the time of these observations, nor were there procedures and programs available to correct for them, so our flux density bootstrapping was accomplished without adjustments for opacity or antenna gain. Because of the slight dependence of these effects on frequency at wavelengths shorter than $\lambda 2$ cm, we do not expect any effect on our spectral index maps made from pairs of these longer wavelengths. At $\lambda 2$ cm, there is a strong differential effect, and we have adjusted the text and figure captions to reflect our recent understanding of the opacity and antenna gain effects.

It is useful to compare our measures of the total flux density of Pictor A (without the attenuation corrections) against the values given in the literature. Examination of the calibrated data showed the 'zero-spacing flux density' of Pictor A at P-band to be 193 Jy, about 9% below the value expected from the spectrum shown in Fig. 1. At $\lambda 20$ cm, the indicated total was 64 Jy, 6%

below the expected value. At $\lambda 6$ cm, no estimate of the total flux density from the visibilities is possible, as the source is heavily resolved by the antenna primary beam. However, after deconvolution and correction by the measured primary beam pattern, the indicated total flux in the $30''$ resolution image was 23 Jy, equal to the expected value. The shortfall at $\lambda 20$ cm is expected by atmospheric attenuation alone, but the excess shortfall at $\lambda 90$ cm and the lack of observed shortfall at $\lambda 6$ cm is puzzling. We can only speculate that the procedures of deconvolution and antenna gain correction have somehow overestimated the total flux density by an amount equal to the shortfall caused by absorption, and that our estimation of the gain variation at $\lambda 90$ cm has not detected a 3% gain loss at low elevations. But the alternate explanation – that the flux differences are real, is also likely. Because of these uncertainties, we have chosen to adjust our images only for the effect of atmospheric attenuation and gain loss, (since these effects are now well established), and not to make further adjustments based on the flux density discrepancies noted above.

If the discrepancies noted in the last paragraph were real, they would result in small necessary adjustments in calculations of the spectral index. It is straightforward to show that if the flux densities at frequencies ν_1 and ν_2 are in error by scale factors f_1 and f_2, respectively, the resulting error in spectral index is $\delta\alpha = \log(f_2/f_1)/\log(\nu_1/\nu_2)$. If the discrepancies were real, our $\lambda\lambda 90\text{-}20$ cm spectral index must be increased by 0.02, and the $\lambda\lambda 20\text{-}6$ cm index by 0.05. We note that the corrections are small, and in any event, the most important information is the change of spectral index across the source on a given image. This change is not affected by any scaling error.

At the extremely low elevations that must be used for these observations, the angular coherence scale is very small. We were thus fortunate to have a phase calibrator as close by as $0537-441$, whose angular offset from Pictor A is only $2^\circ.6$. Although self-calibration can nearly always be counted on to recover the scrambled phase for an object such as this which contains considerable bright, unresolved structures, coherence between the object and a calibrator of known position must occur in order to obtain a position for the target source. As shown in Sect. 4.1.4, sufficient coherence was obtained on enough baselines to allow accurate positions of the nucleus and Western hot spots to be determined with good accuracy.

Calibration of the antenna polarization cannot be done through observations of $0537-441$ alone, since the range in parallactic angle covered by this object is too small. To allow accurate polarization calibration, observations of $0529+075$ were inserted approximately hourly throughout each observing run[4]. The phase difference between oppositely polarized channels (corresponding to the position angle of the polarized electric vector) was set through observations of 3C 138 or 3C 286, whose plane of polarization was assumed to be -12° and 33°, respectively.

Polarization calibration and imaging are very difficult at $\lambda 90$ cm, since there are no strongly linearly polarized objects available to allow calibration of the $R - L$ phases, and because the typical ionospheric rotation measure of a few radians per meter squared results in a rotation of the plane of polarization at 327 MHz of a few turns. Changes in the ionospheric electron content will cause large changes in the apparent plane of polarization. However, we have been able to make good polarization images of Pictor A at this frequency by using the same technique employed by Fomalont et al. (1989) for Fornax A. This technique takes advantage of the existence in Pictor A of bright, compact polarized flux – the hot spot. A single snapshot observation of Pictor A easily detected the polarized flux from the hot spot, so a sequence of snapshot images, for six of the eight separate databases (two frequencies and four configurations) allowed the variation of the rotation of the plane of polarization to be followed and corrected[5]. We have no information on the intrinsic position angle of the hot spot polarized flux at this frequency (the RM determined from higher frequency observations is not sufficiently accurate to allow a prediction of the 327 MHz position angle, and in any event, we cannot prove the measured RM is entirely external, so extrapolation to this frequency may not be valid), so an arbitrary angle of -62° (equal to the high-frequency value) was selected. The results of this process will be shown in Sect. 4.1.5.

After initial editing and calibration, the data from all observing runs were further processed within AIPS[6]. Self-calibration, imaging, and deconvolution were applied following familiar and standard methods (see e.g. Perley, Schwab and Bridle, 1989). For all bands and resolutions, dynamic ranges of a few thousand were obtained.

4. Results

4.1. General source morphology

4.1.1. The lobes

Fig. 3 shows Pictor A at $\lambda 20$ cm with a resolution of $10''$. The source comprises two remarkably round lobes of emission of rather low surface brightness (maximum $I \sim 125$ mJy/beam, i.e. ~ 1 mJy/arcsec^2). The source is $210/h$ kpc in extent, each lobe diameter (transverse) is about $95/h$ kpc. These measures indicate Pictor A to be of average size for a radio galaxy of its luminosity. At the extrema of the lobes are located very pronounced hot spots – a single hot spot at the west end, and a double one at the east. Near the geometric center is an unresolved core, identified with the nucleus of the optical galaxy.

The lobes are remarkable in their roundness: most FR II sources have rather elongated lobes, indicating rapid or preferred growth along one axis, and in some cases, diffuse tails

---

[4] Observations at different frequency bands have been mixed on time intervals of minutes throughout the observations, stretching out the net observing time at a given frequency over several hours.

[5] It was not possible to apply this technique to the DnC-configuration data, since the hot spot could not be separated from the lobe emission.

[6] AIPS is an acronym standing for Astronomical Imaging Processing System, an extensive software package provided by the National Radio Astronomy Observatory for the calibration and reduction of astronomical data.
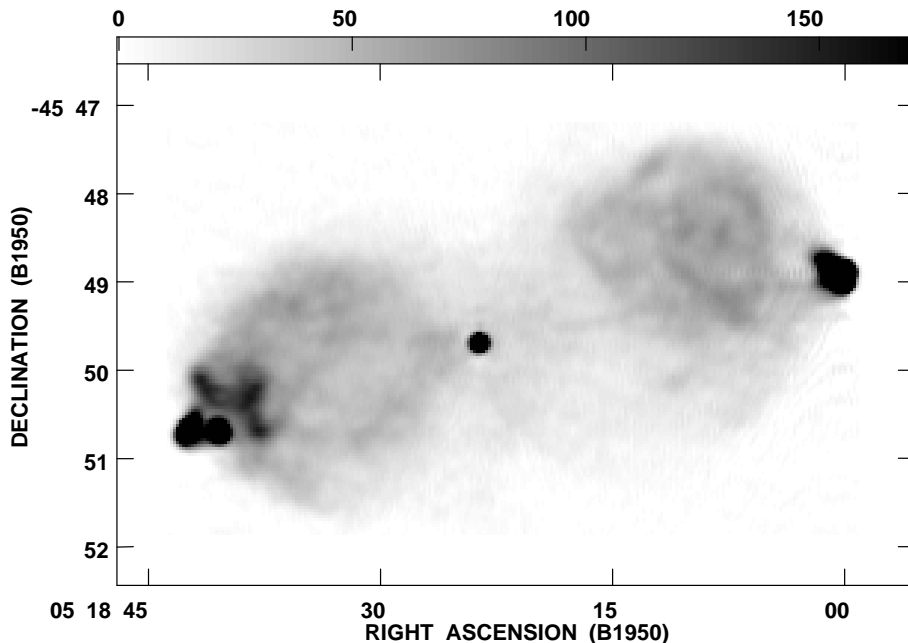
Fig. 3. A grey scale representation of the total intensity of Pictor A at 20 cm wavelength with 7."5 resolution. The grey scale wedge is linear from 0 to 179 mJy/beam, as shown at the top of the figure.

extending perpendicular to the main axis, perhaps indicating back-flow or buoyant effects (Leahy and Williams, 1984), or an ancient axis of ejection. Pictor A's lobes appear very relaxed and round, with an ellipticity of over 0.9 (here defined as the maximum transverse extent over half the total length), perhaps suggesting they are statically confined in a uniform medium. In this, they are reminiscent of the lobes of Fornax A (Fomalont et al. (1989), an extremely relaxed radio galaxy often considered to be a 'dying' radio source. Whereas the roundness of its lobes suggests that Pictor A is quietly expanding (i.e. no longer expanding along the source axis), the presence of its extraordinary hot spots suggests that it probably was recently re-activated. In that respect, Pictor A is a very different radio source than Fornax A. In fact, the association of such prominent hot spots with such diffuse lobes is very unusual amongst radio galaxies.

Most regions of the lobes are relatively featureless which, combined with the complete absence of any limb brightening, indicates that the emitting material is rather uniformly distributed throughout the visible volume. However, in parts of both lobes, thick filaments are found, although they are prominently seen only in part of the western lobe. Here, there are three dominant filaments, roughly elliptical in shape, of approximately $50/h$ kpc in maximum diameter. These filaments are rather thick, being about $5/h$ kpc in size, and with excess surface brightness of about 0.5 mJy/arcsec^2 at 1465 MHz. The distribution of these finer scale features is better visible in Fig. 3, showing a grey scale representation of the source at 7."5 resolution at λ20 cm. Filamentary structure is now recognized as being common in the lobes of radio galaxies, having been detected in detailed VLA radio imaging of nearly all the best-known radio sources: Cygnus A (Perley et al. (1984), Virgo A (Hines et al., 1989), Fornax A (Ebnetter et al., 1989), Hercules A (Dreher and

Feigelson, 1984), 3C 310 (van Breugel and Fomalont, 1984), and 3C 219 (Clarke et al., 1992).

4.1.2. Spectral index of the lobes

The general run of the spectral index is best seen at a resolution of 30″, where images taken at a frequency of 327 MHz are available, and where the resolution is low enough to smooth out the filamentary features in the lobes. Fig. 4 shows Pictor A contoured at the same levels relative to the peak (i.e. the western hot spot) at $\lambda\lambda$90, 20, and 6 cm, respectively. There is striking similarity between these maps, the major difference being the appearance of the radio nucleus at shorter wavelengths. Closer inspection reveals a second important difference – the λ6 cm image is distinctly more 'narrow-waisted' than either of the two longer-wavelength images, indicating spectral steepening in the regions near the radio nucleus. The steepening is evident in images of spectral index, shown in Fig. 5. To more clearly show the lobe spectral index, we have removed the nuclear source by subtraction of a point source of the flux density and position indicated from high resolution images at each band. Small residual errors in this process result in the small-scale perturbations in spectral index seen near the location of the nucleus. The upper panel in Fig. 5 displays the spectral index α_{20}^{90} showing the uniformity of the spectral index throughout the broad lobes ($\langle\alpha\rangle$ = 0.80), except for a slight flattening towards the hot spots and some steepening in the central regions, especially along the N and S edges. Note also the eastern lobe has a generally steeper spectrum than the western (see Sec. 5.1). The lower panel in Fig. 5 displays the spectral index α_6^{20} and shows the steepening along the periphery and in the central regions much more clearly. The spectral index in these regions exceeds 1.7, and undoubtedly is much higher in those regions where we are
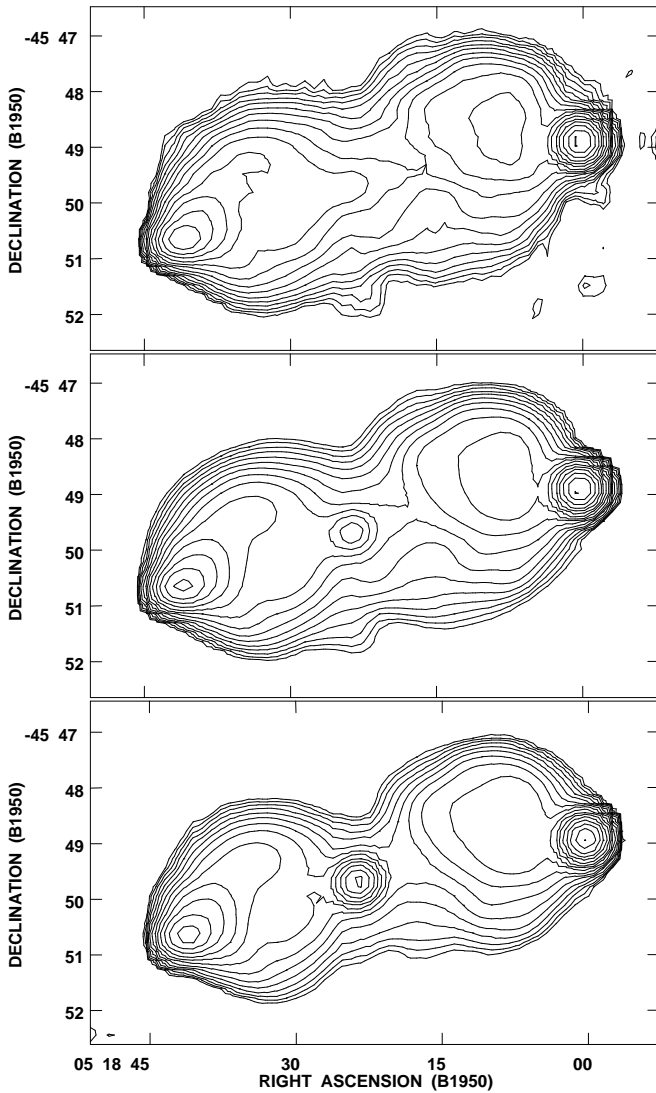
Fig. 4. Pictor A at $\lambda 90$ cm (top), $\lambda 20$ cm (middle), and $\lambda 6$ cm (bottom), contoured identically with levels between 0.4 and 72.41,% of the peak intensities of 23.0, 9.61, and 4.56 Jy/beam, respectively. Intensity ratio between contours is $\sqrt{2}$.

Fig. 5. Spectral index maps of Pictor A at $30''$ resolution. The top figure shows α_{20}^{90}, the bottom α_6^{20}. Grey scale for the spectral index extends from 0.5 to 1.7.

unable to detect extended emission at $\lambda 6$ cm due to insufficient brightness sensitivity. Note also that the contours of constant spectral index are approximately circular in both lobes, especially the western, indicating that the spectrum is much steeper along the edges than in the center. An identical result has also been reported in Cygnus A by Carilli et al. (1991).

However, these notable changes in lobe structure with frequency are not evident at the lowest frequencies. Fig. 6 shows Pic A at 73.8 and 327 MHz at a resolution of $45''$ by $150''$. The lobe emission at this pair of frequencies is very similar, and the only notable difference between the images is due to the slightly flatter spectral index of the western hot spot. The strong spectral steepening seen between $\lambda 90$ cm and $\lambda 6$ cm suggests that the lobes should appear vastly different at shorter wavelengths, and also indicates that much can be learned about the ageing pro-
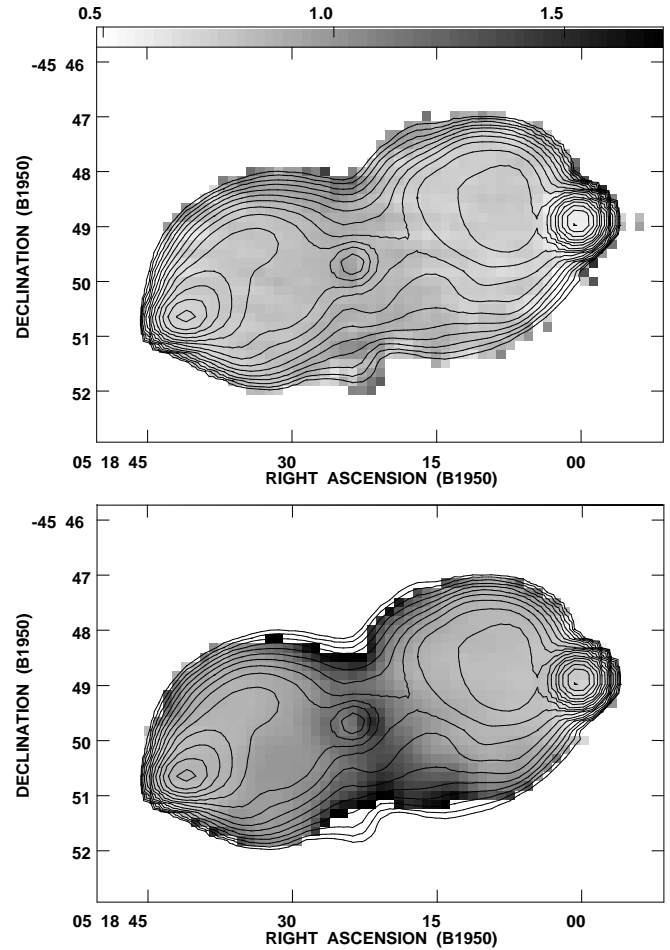
cess through imaging at such wavelengths. Unfortunately, our current data cannot test these expectations. At $\lambda 3.6$ cm, we have only A- and BnA-configuration data, which have poorly sampled spacings less than about 7000 wavelengths. Structures on scales larger than about $5''$ cannot be reconstructed with these data, so observations in more compact configurations are required. At $\lambda 2$ cm, we have fairly good coverage down to about 1500 wavelengths, so images with as low as $30''$ resolution should recover the brightness on scales up to perhaps half the primary antenna power pattern – about $150''$. However, Pictor A is much larger than this, so full brightness imaging will require mosaicing, which is a difficult project for an object of this declination. Our only pointing at this frequency is on the hot spot, so obviously there can be no recovery of the low brightness, extended emission at separations exceeding about one arc minute.

However, we do have an indication of extreme spectral steepening in regions close to the western hot spot. Fig. 7 shows the spectral indices between $\lambda 20$ cm and $\lambda 6$ cm (upper panel), and between $\lambda 6$ cm and $\lambda 2$ cm (lower panel) at $10''$ resolution. The former image shows nearly no steepening between the hot spot and adjacent lobe, while the latter shows drastic steepen-
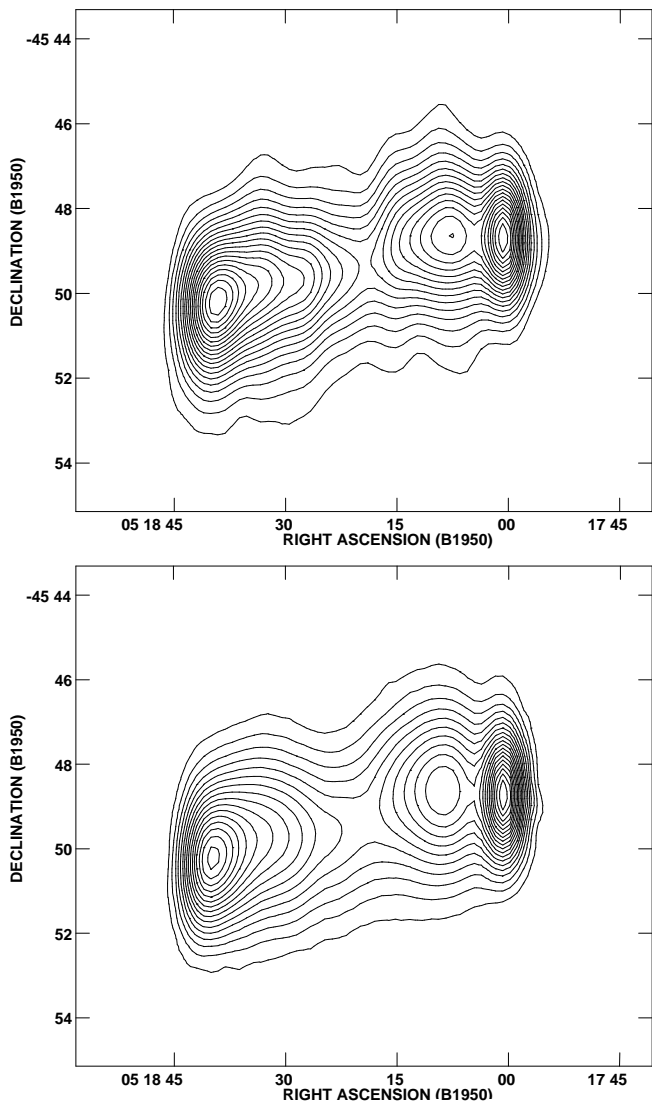
Fig. 6. Maps of Pictor A at a wavelength of 4 meters (top) and 90 cm (bottom), at a resolution of 45″ by 150″.

Fig. 7. Spectral index distribution in the vicinity of the western hot spot of Pictor A. The upper panel shows α_6^{20} at 20″ resolution and the lower α_2^6 at 10″ resolution. Contours are also for the spectral index with 0.1 increments for both panels. The grey scale is the same for both, extending from 0.6 (white) to 1.2 (black). The angular scale is the same in each image.

ing, from about 0.6 on the hot spot to 1.5 in the regions on the eastern side of the hot spot. Beyond 20″ from the hot spot, there is no measurable lobe emission at $\lambda 2$ cm. An image at this wavelength with 20″ resolution shows no sign of emission from the lobes at separations exceeding 20″ from the hot spot. Investigations of this steepening will require low-resolution observations at $\lambda 3.6$ cm, which we will undertake in the near future.

The spectrum of the hot spots proper will be discussed in Sect. 4.2.2, and a discussion of the implications of the measured steepening will be found in Sect. 5.

4.1.3. Is there a jet?

The jet is very faint and best seen on a TV monitor. A reasonable representation by grey scale is given in Fig. 3, showing the source at 7″5 resolution at $\lambda 20$ cm. The jet extends along p.a. $-78°$ until a small bend about 180″ from the nucleus, be-
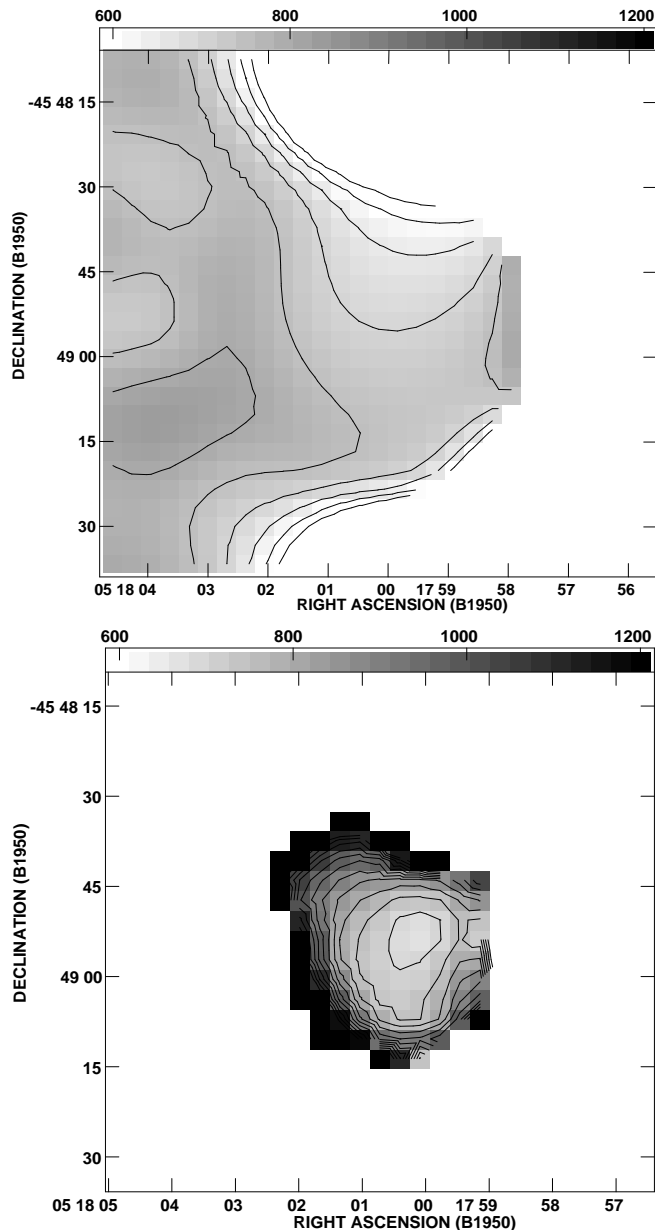
yond which the jet proceeds along p.a. $-85°$ until it reaches the Western hot spot. The average excess brightness of the jet above the background lobe emission is estimated to be about 10 mJy/beam at $\lambda 20$ cm. No accurate estimate of the jet's width is possible, but it is clearly not greatly resolved by the 7″5 beam. The flux density of the entire jet is estimated to be 335 mJy at $\lambda 20$ cm, or approximately 0.5% of the total. The jet/counter-jet ratio is greater than three. The jet is also faintly seen at $\lambda 6$ cm and $\lambda 90$ cm.

Many arcsecond jets have detectable jets on milliarcsecond scales. For a number of cases, the 'inner jets' can be seen on sub-arcsecond VLA images made at $\lambda 3.6$ cm or $\lambda 6$ cm. We have searched carefully for such extensions of a sub-arcsecond jet, but have found nothing to a limit of 0.3 mJy/beam in the vicinity of the nucleus.

4.1.4. Nucleus and radio astrometry

The radio core emission is unresolved at all wavelengths and resolutions. We have been able to obtain an accurate position because the proximity of the astrometric phase calibrator $0537-441$ allows good phase bootstrapping. The X-band observations taken on 10 October 1991 in the BnA-configuration were of remarkably good phase stability, with short time-scale fluctuations of not more than $20°$ per minute on all baselines superimposed onto a longer time-scale phase gradient which increases with baseline length. Examination of phase differences between the calibrator and the Pictor A nuclear source showed phase coherence (defined as maximum phase differences being less than 1 rad) on baselines shorter than about 3 kilometers. Consequently, we determined the position of the nuclear core, using only data from baselines shorter than this value. We find:

$$\alpha_{\text{radio}}(1950) = 5^h\,18^m\,23^s\!.590 \pm 0^s\!.01,$$
$$\delta_{\text{radio}}(1950) = -45°\,49'\,41''\!.40 \pm 0''\!.05.$$

The quoted error estimates have been determined in three ways: First, the AIPS program IMFIT was used to determine both the position and its estimated error. Tests demonstrated the program gives reasonable error estimates if the image is not oversampled. Second, we used Fomalont's (1989) estimator of the accuracy of the position of an unresolved object: $\sigma \sim \theta/(2\,\text{SNR})$, where θ is the resolution and SNR is the ratio of the peak flux to the rms noise. Third, recognizing that estimation of a position is equivalent to a linear regression of phase with baseline with the slope being proportional to the positional offset allows derivation of a simple expression relating the positional error to the uncertainties of the phase measurements: $\sigma = \sqrt{2/N}/\beta$, where N is the number of independent measures of the phase, and β is the baseline length (in wavelengths) where the rms-phase error is 1 radian. All three methods returned similar estimates – the values quoted above are the means. These results are in excellent agreement with our independent results obtained from the L- and C-band data.

We compare this radio value to our optical determination, based on a CCD frame taken with EFOSC I at the ESO 3.6m-telescope:

$$\alpha_{\text{opt}}(1950) = 5^h\,18^m\,23^s\!.66,$$
$$\delta_{\text{opt}}(1950) = -45°\,49'\,42''\!.2.$$

with a measured 1-σ error of $0''\!.25$ for the primary reference frame (i.e. *rms* scatter in the positions of the PPM primary reference stars). The angular difference between optical and radio position is $1''\!.1$, i.e. considerably larger than the formal error. This might well be due to the fact that the optical nucleus is

Table 2. Flux densities of the nucleus of Pictor A

Band	Frequency [MHz]	Flux Density [Jy]
P	330	$0.68 \pm .05$
L	1470	$1.10 \pm .05$
C	4850	$1.15 \pm .05$
X	8440	$1.10 \pm .05$

clearly extended and thus its centroid need not coincide with the radio nucleus. In addition there might be an offset between the radio and the optical reference frame. We do not believe the difference is due to the radio determination, because interferometric observations are blind to first order (planar) diffraction, and the smaller second order effects (due to atmospheric curvature) are largely eliminated by use of a reference source at the same declination as Pictor A.

The flux density of the radio nucleus is given in Tab. 2 for each of the observing bands. From this it will be noted that the nucleus has a flat spectrum, with a slight inversion at the longer wavelengths.

Our data reduction technique combined different configurations without imaging each one, in order to save time. An unfortunate consequence of this methodology is the loss of information on time variability of the core. We have recognized the error in this procedure, and reduced and imaged the X-band observations separately, before combination. We find that the nuclear flux density at 8.7 GHz declined from (1.10 ± 0.03) Jy in March 1990 to (1.00 ± 0.03) Jy in October 1991. The estimated error comes from our experience in bootstrapping flux densities at a variety of bands. This error is dominated by small residual pointing errors. Both of these data sets were taken in very dry, calm weather. To ensure that we were not seeing a change in system gain, we compared this change to that seen in the two calibrators: $0537-441$ showed a flux density increase over the same time: from 3.93 to 4.05 Jy, while 0529+075 showed a larger flux density increase, from 1.86 to 2.34 Jy. Both of these variations are significant and neither is unusual for flat spectrum sources. We are thus confident that the variation seen in the nucleus of Pictor A is intrinsic to the source.

4.1.5. Polarization structure

Early observations of Pictor A with low resolution found a rather low degree of polarization. Our higher resolution observations indicate why: Fig. 8 shows the polarization structure at $\lambda 6$ cm superposed on total intensity isocontours for reference. The dashes are proportional in length to the degree of polarization, their orientation gives the position angle of the projected **E**-vector. A clockwise rotation of $10°$ has been added to account for the mean rotation measure (see Sec. 4.1.6). The results show that the projected magnetic field lines are accurately aligned with isocontours of surface brightness around the radio lobes. This geometry will result in an effective cancellation of the polarization if observed with resolution on the scale of, or larger
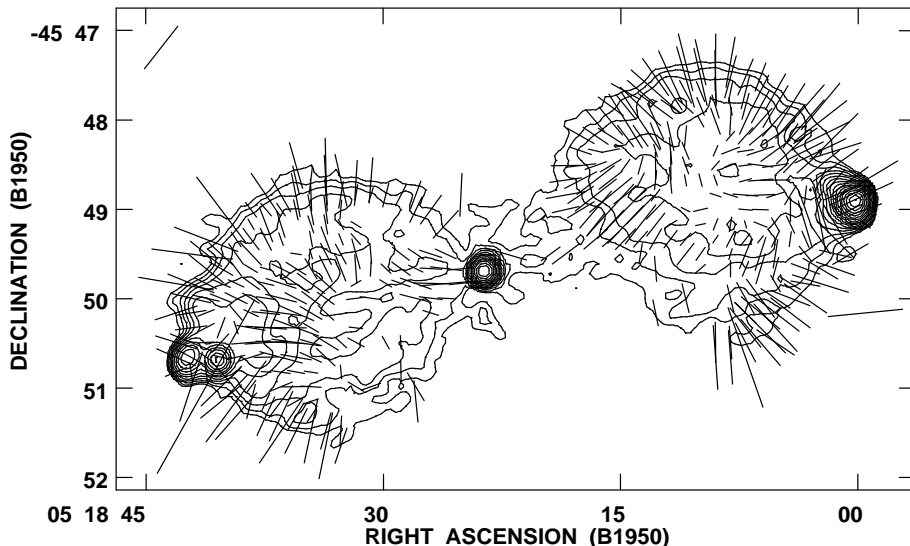
Fig. 8. The polarization structure in the lobes of Pictor A, at 6 cm wavelength and 10″ resolution. The contours are drawn at 0.4 to 72.4 % of the peak brightness of 3.21 Jy/beam with a spacing ratio of $\sqrt{2}$. The dashes show the direction of the observed **E**-vector, corrected for a foreground RM of 45 rad m^{-2}. The projected **B**-vectors are normal to the dashes. The length of the dash is proportional to the degree of polarization, a length of 1″ indicates a polarization of 1%. The dominant magnetic field structure is circumferential, as in most radio sources. The filaments seen in Fig. 3 do not, in general, display magnetic fields along their length.

than the radio lobes. The close alignment of the projected fields and brightness contours is a very common characteristic in extragalactic radio sources.

A notable feature is the enhancement of the degree of polarization around the edges of the lobes, particularly the western one. This is evident in Fig. 9, showing grey scale representations of the degree of polarized flux density at 10″ resolution at λ20 cm (top) and λ6 cm (bottom) respectively. In both images, pixels whose degree of polarization has been determined with a SNR (signal-to-noise ratio) less than 5 are blanked. The edge enhancement is again a common characteristic in radio galaxies. Around this edge, the degree of polarization is between 30 and 60 %, but in the center of the lobes, values of 10 to 20 % or lower are more common. Regions of very low polarization are found at both $\lambda\lambda$6 and 20 cm, and are probably due to cancelation along the line of sight. This interpretation is given considerable weight by the similarity of the polarization patterns between the two frequencies, especially in the western lobe. The polarized flux is distributed in filaments, as shown in Fig. 10, a grey scale representation at 10″ resolution at λ20 cm. Comparison of this figure with Fig. 3 shows little correlation between the polarized filaments and those of total intensity.

In observations of Cygnus A (Perley et al., 1984), and in Virgo A (Hines et al., 1989), it was reported that projected magnetic fields appear to be closely aligned with the observed brightness filaments. This does not appear to be the case for the thick filaments in Pictor A, as can be seen by comparing Fig. 8 with Fig. 3.

In Sec. 3 we described our method for removing the ionospheric rotation from the polarized images of Pictor A at 327 MHz. The results of this are presented in Fig. 11 with 30″ × 6″ resolution. The lower panel shows that both lobes are extensively polarized at λ20 cm, with the western lobe showing a higher degree of polarization than the eastern lobe. The corresponding picture at λ90 cm is in the upper panel of Fig. 11.

Note that the polarization of the western lobe remains high, but the eastern lobe is completely depolarized.

Although the eastern lobe is significantly polarized at λ90 cm, the average degree of polarization is considerably reduced from the values measured at higher frequencies. It is not clear if this is due to internal depolarization due to gas within the lobes, or is caused by unresolved RM-fluctuations in a foreground screen. This point is further discussed in Sect. 5.3.

4.1.6. Rotation measure

Table 1 shows that the λ20 cm data were taken at two adjacent frequencies – 1446 and 1496 MHz. Although these are close, they are sufficiently separated to allow determination of the Rotation Measure RM. The resulting image, using only position angle data whose error was less than 5°, shows a patchy distribution of RM across the source. The magnitude of the fluctuations is $\sim$ 10 rad m^{-2}, and is accountable by measurement errors in the position angle maps combined with the proximity of the two observing wavelengths. The mean value, for both lobes, of $RM = (43.5 \pm 1.4)$ rad m^{-2}, is in excellent agreement with past work. The mean RM for each lobe separately is the same within the quoted errors. The rotation measure gradient cannot exceed 0.4 rad m^{-2} per arcminute. No significant variations in the RM of the type seen in conjunction with hot spot B in Cygnus A (Dreher et al., 1987), or 3C 194 (Taylor, 1991), or in many other radio sources as shown by Zukowski (1990) are seen near the hot spots of Pictor A.

All position angle images of the lobes have been corrected for the RM structure. However, no corrections were made to images of the hot spots since the maximum correction needed is less than 10° at λ6 cm, and is negligible at shorter wavelengths.

The RM-image determined from the λ20 cm data alone suffice to show the general trend over the radio source, but the results obtained are not accurate enough to enable a prediction of the λ90 cm polarization, or to determine the scatter of the

Fig. 10. A grey scale image (range 5 to 50 mJy/beam) of the polarized intensity of Pictor A at a wavelength of 20 cm and resolution of $10''$.
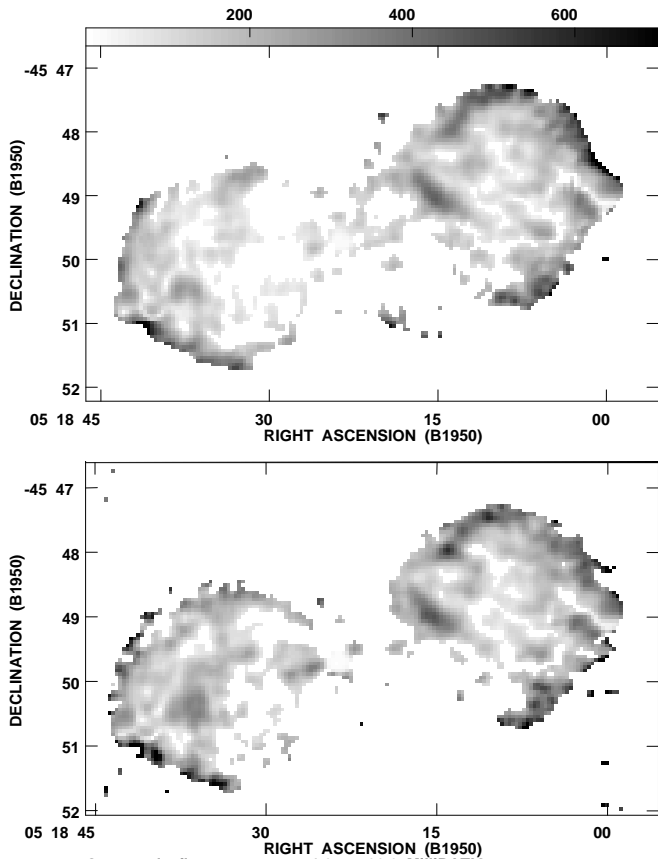
Fig. 9. Greyscale representations of the degree of polarization of Pictor A at $10''$ resolution at 20 cm wavelength (top), and at 6 cm wavelength (bottom). The grey scales are the same in both, linear from 0 to 70 %.

age, corresponding to an RM of 48.9 rad m^{-2}. This procedure minimizes the angle difference between the λ20 cm and λ6 cm images. The resulting image was subsequently incremented by this same value, to recover the proper zero point. This final image is shown in Fig. 12, and shows that the RM in both lobes is very similar: 49 rad m^{-2} in the west lobe, 46 rad m^{-2} in the east lobe. But more significant is the variation in the RMs in these lobes. Histograms of the measured RMs, shown in Figs. 13, show closely Gaussian distributions with very different widths: 4.9 rad m^{-2} and 10.2 rad m^{-2} for the western and eastern lobes, respectively.

4.1.7. Depolarization

Fig. 9 clearly demonstrates the similarity of the polarization at L- and C-bands at $10''$ resolution. This alone indicates the depolarization of the radiation is not extensive. To quantify this indication, we constructed depolarization images by dividing the degree of polarization at λ20 cm by the corresponding image at λ6 cm. To ensure reliable results, only polarization values with signal-to-noise ratio exceeding five were used. The results show that the depolarization is small in the western lobe, but significantly higher in the eastern lobe (see Fig. 14). The simple mean of the depolarization ratio of the western lobe is $0.96\pm.01$, while for the eastern lobe the mean value is $0.76 \pm .01$ (a value which is skewed upwards by our inability to measure very low values of depolarization).

This trend is clearly continued to 327 MHz, where the eastern lobe is completely depolarized at the $6 \times 30''$ resolution level, while significant areas of the western lobe remain polarized at this resolution. These results are consistent with the 'depolarization asymmetry' found by Laing (1988) and by Garrington et al. (1989), (1991). In Sect. 5.3, we discuss whether the complete depolarization of the eastern lobe is consistent with an interpretation of a deeper foreground screen in front of that lobe.

RM over the lobes. To accomplish these, we must employ observations taken over a wider frequency range. Because both lobes show significant polarized flux at both λ6 cm and λ20 cm wavelengths, a rotation measure image can be constructed using these data, provided the range of RM within the lobes is less than ±40 rad m^{-2}. Larger values will cause a differential rotation between λ6 cm and λ20 cm of more than 90°, making interpretation of a resultant RM-image impossible. Fortunately, the range in RM, as shown by the L-band data alone, is less than this over most regions of both lobes, giving us confidence that the RM-image resulting from the L and C band data will not suffer from rotation ambiguities. It is also required that the resolution at the longer wavelength does not smooth the position angle variations of the polarized emission – a process which would narrow the distribution of the derived rotation measures. But neither can we use too high a resolution for our RM determination, since this will lose the polarized brightness we need to make the determination. By trial, we have determined the optimum resolution (a balance between undue smoothing of the longer wavelength polarized emission, and over-resolution of the shorter wavelength emission) to be $10''$. The resulting image was made by first subtracting 110° from the λ20 cm-p.a. im-
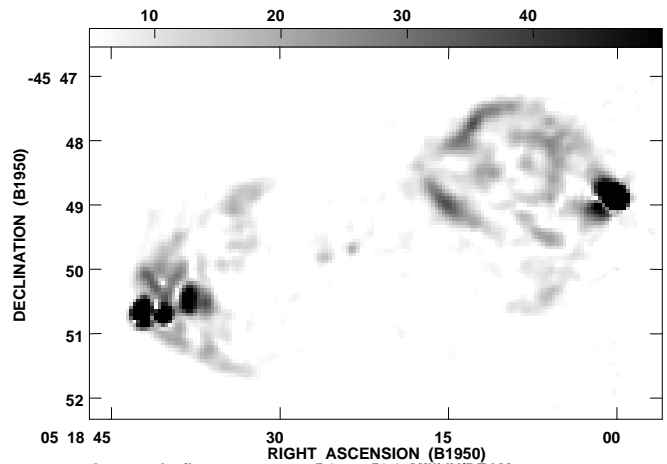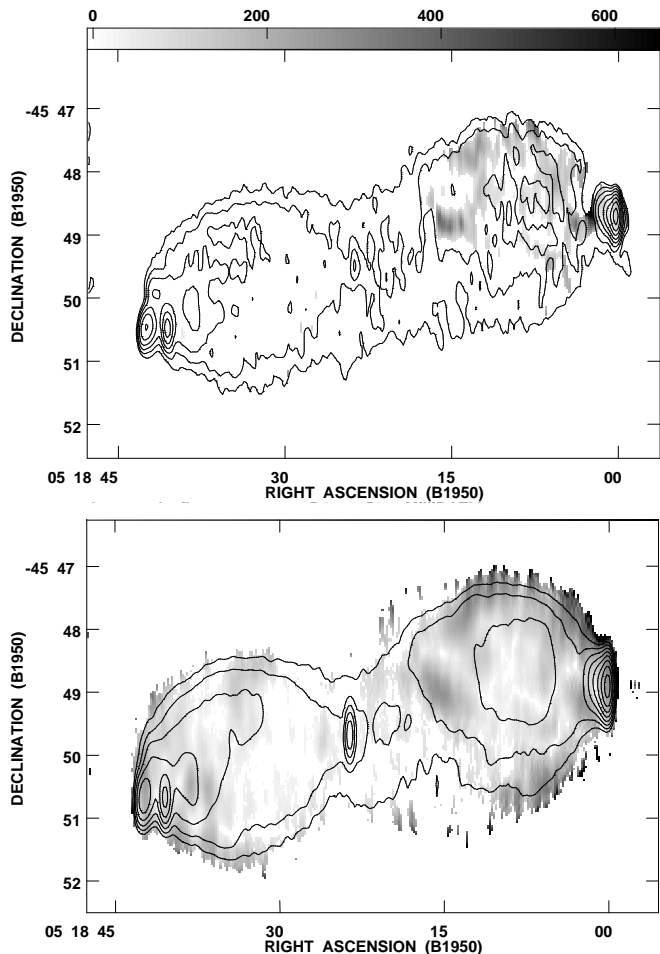
Fig. 12. Rotation measure RM from the $\lambda 20$ cm and $\lambda 6$ cm maps at $10''$ resolution. Contours are at $\lambda 6$ cm spaced by a factor of 2 between 0.552 and 70.71 % of the peak flux of 3.01 Jy/beam and grey scale extends from 30 to 80 rad m^{-2}.

Fig. 11. Degree of polarization across Pictor A at $\lambda 90$ cm (top) and at $\lambda 20$ cm (bottom) at a resolution of $21''.2 \times 4''.9$. Contours are spaced a factor of 2 between 0.552 and 70.71 % of the peak flux of 17.3 Jy/beam in both images and grey scale ranges from $-.5$ to 65 %.

Fig. 13. Histograms showing the different dispersions in the rotation measure RM in the two lobes of Pictor A (eastern lobe to the left).

4.2. Radio structure of the hot spots

Pictor A comprises two distinct morphological components, the diffuse lobes and the compact hot spots. Fig. 3 demonstrates clearly how different these are – even at $10''$ resolution, the brightness ratio between the prominent hot spot and the lobes is nearly 100. In this subsection, we discuss in detail the structure of the two hot spots.

4.2.1. Eastern hot spots

Fig. 3 shows that the Eastern hot spot is actually double. Fig. 15 shows these hot spots at $1''.5$ resolution – the highest possible at $\lambda 6$ cm with a circular beam. The outer hot spot is seen to be completely resolved, while the inner component shows some minor substructure, mainly on the eastern edge. Laing (1989) showed that in general when a double hot spot is seen, the inner one is the most compact. Our observations of Pictor A are in agreement with this relation. This inner hot spot is completely resolved out on higher resolution images – thus there is no de-
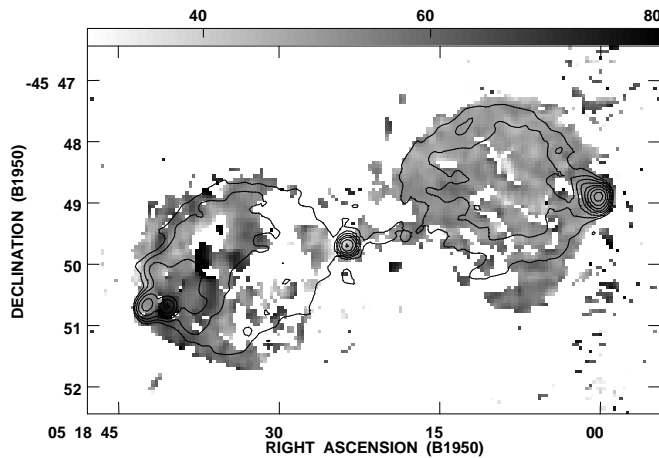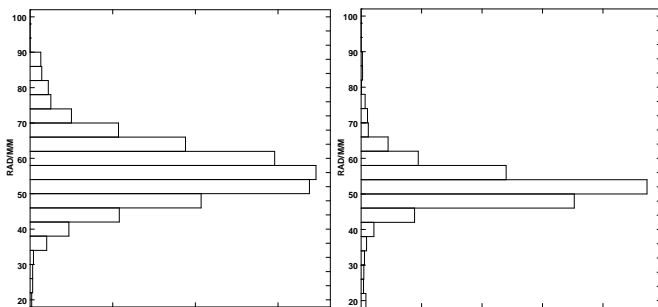
tectable structure on scales less than about 1 kpc in either hot spot.

The polarization characteristics are also included in Fig. 15. Displayed are the projected electric field vectors at $\lambda 6$ cm. The projected magnetic fields are oriented at right angles to the dashes. The eastern (outer) knot displays normal behavior of the apparent field – the **B**-field follows the isointensity contours. However, the westernmost (inner) knot of the pair displays rather unusual projected magnetic structure, with a radial field on the apparent leading edge. In the inner regions of this hot spot, the apparent field behaves in a normal pattern, following the lines of constant brightness. The simplest explanation for the anomalous behavior of the polarized emission on the inner knot is that the fields have been rotated by Faraday rotation through an intervening magnetized cloud. However, we do not feel this is possible in this case, as the required RM to rotate the vectors by 90° at 6 cm wavelength exceeds 400 rad m^{-2}. Such an RM must have observable consequences at 20 cm wavelengths – at the very least, severe depolarization must be seen around the periphery of the cloud due to transverse ('beam') depolarization. Although depolarization is observed, it is small, and general
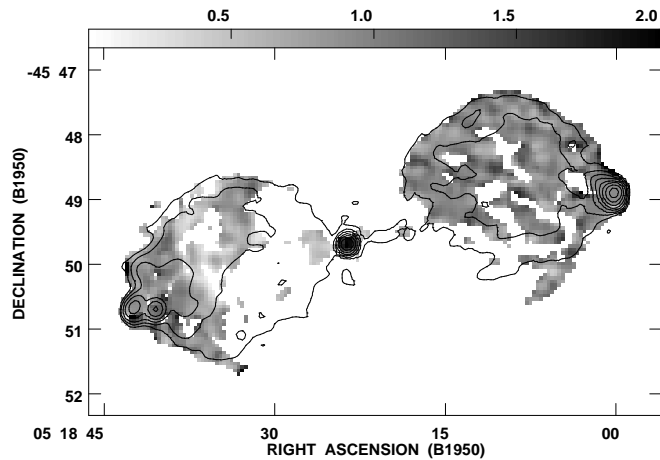
Fig. 14. The depolarization ratio across Pictor A between the $\lambda 20$ cm and the $\lambda 6$ cm degree of polarization at $10''$ resolution. The grey scale wedge is linear, from 0 to 2. Values less than one represent depolarization, values greater than one are *repolarization*, and are nearly all found in regions of low signal. We believe most of these are false. The generally higher depolarization of the eastern lobe is easily seen. Contours are at $\lambda 6$ cm spaced by a factor of 2 between 0.552 and 70.71 % of the peak flux of 3.01 Jy/beam and grey scale extends from 0 to 2.

Fig. 15. Structure and polarization of the eastern hot spots of Pictor A, seen at $\lambda 6$ cm wavelength and $1''5$ resolution. The intensity contours are spaced by $\sqrt{2}$ between 6.25 and 70.71 % of the peak brightness of 74.9 mJy/beam. These hot spots are well resolved at this resolution. The dashed lines represent the **E**-field orientation, and have been corrected for the effect of the foreground rotation measure. The length of the dashed lines is proportional to the degree of polarization, with $1''$ length representing 13.3 % polarization.

throughout the lobe. Another explanation is that the anomalous field is the result of internal depolarization – however, this must result in total depolarization at $\lambda 20$ cm, which is not seen. We thus conclude the anomalous fields are intrinsic, but cannot suggest a reason why they are different from the norm. We note in passing that there is a very faint optical object of unknown origin coinciding within the errors with the region of anomalous magnetic field (Röser, 1989).

The degree of polarization of the eastern knot is very high along the outermost edge – up to the theoretical maximum of 70 %, but drops to rather low values (typically 20 %) on the western side of the eastern knot. The western knot has a more complicated pattern, with high polarization on both the western and eastern edges, but very low in the middle. This is clearly caused by field cancellation across the observing beam, due to the sudden transition in the field geometry.

It is not possible to calculate depolarization at this resolution as no image of this resolution is possible at L-band, and the region lies well outside the U-band primary beam. However, Fig. 14 giving the depolarization ratio between $\lambda 20$ cm and $\lambda 6$ cm at $10''$ resolution, shows the hot spot region has no anomalous depolarization on that angular scale.

The spectral index map (not shown) of α_6^{20} with a resolution of $10''$ does not show any discernible difference between the spectral index of the surrounding lobes and that of these two hot spots.

4.2.2. Western hot spot

The western hot spot is the single most outstanding feature in this radio source. The lower resolution maps (e.g. Fig. 3) show it protrudes by about $4''$ from the lobe. This characteristic is quite
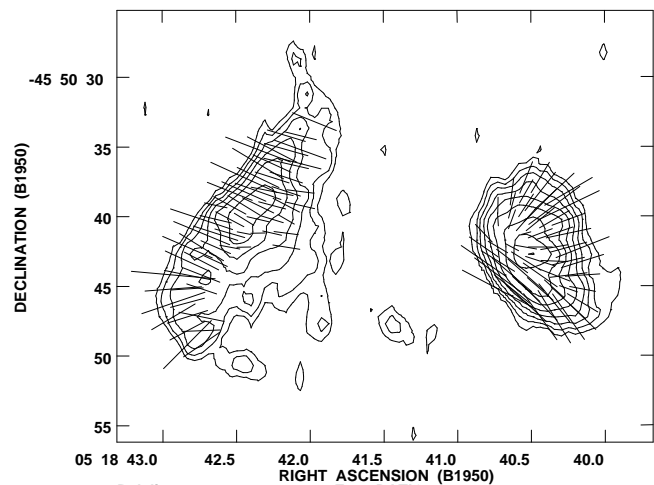
common – it is seen also, for example, in Cygnus A (Perley et al., 1984), and in several of the images presented by Leahy and Perley (1991) and by Black et al. (1992).

Total Intensity   Fig. 16 shows the total intensity structure of the western hot spot at $\lambda 3.6$ cm and $1''5$ ($700/h$ pc) resolution. The hot spot region (seen in Fig. 3 as the westernmost black knot) is seen to comprise two distinct components: A very compact, partially resolved knot, and a plateau region[7], of $25''$ ($14/h$ kpc) length, oriented at p.a. $32°$. The plateau region can itself be considered comprised of two parts, an inner region of length $14''$ ($6.3/h$ kpc) which is also detected at optical wavelengths (see Fig. 22), and an outer, much fainter region extending northwards and eastwards which gradually blends into the general lobe emission. In addition, a low brightness extension towards the core is seen, both in this total intensity image, and in the polarization images (see Sec. 4.2.2 below). This feature is noted also at $\lambda 6$ cm and $\lambda 2$ cm, and we tentatively associate it with the incoming jet.

The radio data are capable of providing images of much higher resolution, as in Fig. 17, showing the hot spot region at $0''77$ by $0''17$ resolution at $\lambda 3.6$ cm. Two new tendencies are shown: The hot spot region remains unresolved on its outer (western) edge, while the inner (eastern) edge is now seen to be resolved, and the plateau region is shown to comprise distinct filaments with widths typically $\sim 1''$ (0.5/h kpc). The vertical elongation of the hot spot is real, and not an artefact of the elliptical beam, as may be seen by comparing its extent with the beam size.

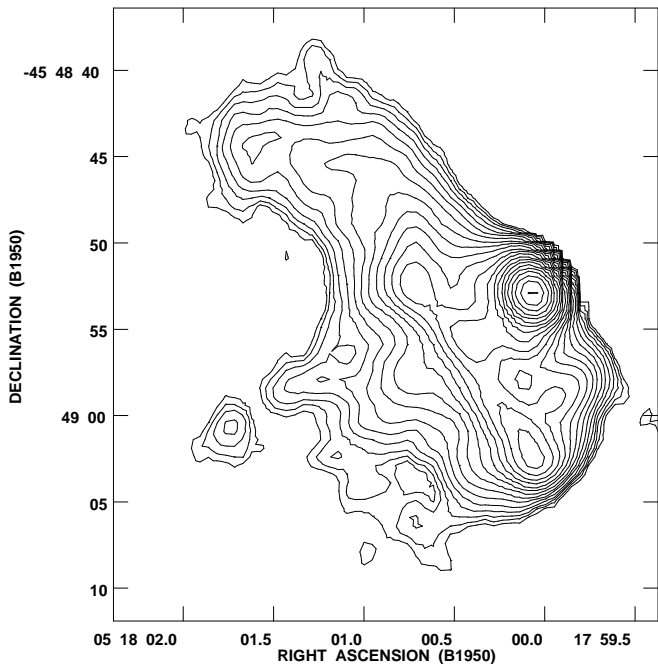[7]   Röser and Meisenheimer (1987) called this the *filament*

Fig. 16. The western hot spot at 3.6 cm wavelength and $1.''5$ resolution. The contours are spaced by a factor of $\sqrt{2}$ between 0.071 and 70.71 % of the peak intensity of 0.94 Jy/beam.

Fig. 17. The western hot spot of Pictor A at $\lambda 3.6$ cm $0.''8 \times 0.''2$ resolution. Contours are spaced with a factor of $\sqrt{2}$ between 0.552 and 70.71 % of the peak intensity of 215 mJy/beam.

The sharp leading edge of the hot spot allows an estimate of the incoming jet angle (presuming the emission to be normal to the jet axis). This is found to be p.a. $-70°$, within $15°$ of the measured jet closest to the hot spot, and within $8°$ of the much larger section of the jet seen in Fig. 3 to be extending from the nucleus.

The A-configuration observations taken in March 1990 allowed images of the hot spot at $\lambda 2$ cm, with the maximum resolution of $0.''47$ by $0.''09$ (200/h by 41/h pc), given in the upper panel of Fig. 18. This image shows the hot spot itself is formed of two regions – a narrow, still unresolved region approximately $0.''5$ in width and $1.''5$ in extent, and a plateau, extending backwards toward the nucleus about $1''$, which has a sharp brightness gradient on the inner (core-ward) side.

In the lower panel of Fig. 18, we show the result of deconvolving the image with the AIPS program VTESS, which applies the maximum entropy method (MEM). Experience has shown that in regions of good signal-to-noise, deconvolutions by this method will safely superresolve by about a factor of three. We have used VTESS to super-resolve also our X-band image, and find results which are comparable to those shown in the lower panel of Fig. 18, although the resolution achieved is not sufficient to reproduce the parallel ridges. Our result at $\lambda 2$ cm uses a cell size of $0.''025$, (11 pc), and we are confident that the structures seen in the VTESS-image on this scale do represent reality. This figure shows that the brightest region of the hot spot's leading edge is (again) comprised of two regions, but in this case, the two regions are nearly parallel ridges of extreme thinness ($0.''075$, or $35/h$ pc), with approximate length of $1''$.
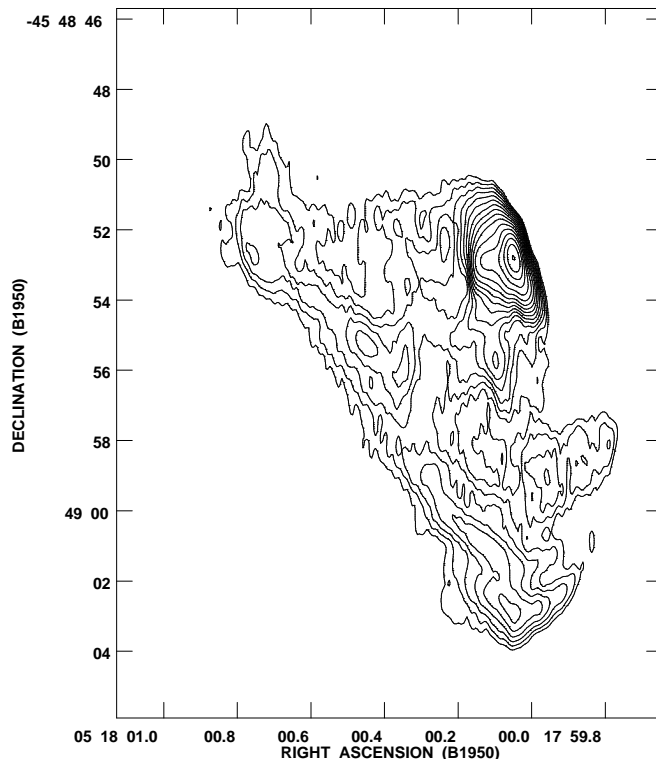
The two ridges are oriented at $\sim 11°$ (inner) and $\sim 16°$ (outer). Note that the inner ridge is oriented within $1°$ of the normal to the angle of the jet seen extending from the nucleus, and within $8°$ of that portion which appears to be feeding the hot spot, as seen in Fig. 16. The peak brightness of the hot spot ridge is very high – 1.22 mJy/cell, or 2.05 Jy/arcsec^2. Assuming a spectral index of 0.7 (to be justified in the next section), the $\lambda 6$ cm peak brightness is 3.85 Jy/arcsec^2.

Spectral Index At all frequencies between 74 MHz and 5000 MHz, the data are consistent with the spectral index of the western hot spot region being flatter by only 0.1 to 0.15 than the the nearby lobe emission. There is a hint that this flattening is less pronounced at higher frequencies and more pronounced at lower frequencies. The mean spectral index of the western hot spot is 0.6 to 0.7, with the uncertainty due to our difficulties in establishing the flux density scale.

The spectral index of the hot spot region steepens only slightly between $\lambda 6$ cm and $\lambda 2$ cm, increasing to approximately 0.7 from its low frequency value of 0.6 to 0.7. Of great interest is the spectrum of the filamentary plateau region, since this is located some $3.3/h$ kpc from the hot spot. Fig. 19 shows α_2^6 with $4''$ resolution, from which it will be seen that the spectral slope of the filament is steeper than that of the hot spot proper by $\Delta\alpha \gtrsim 0.1$ (see also Sec. 5.2).
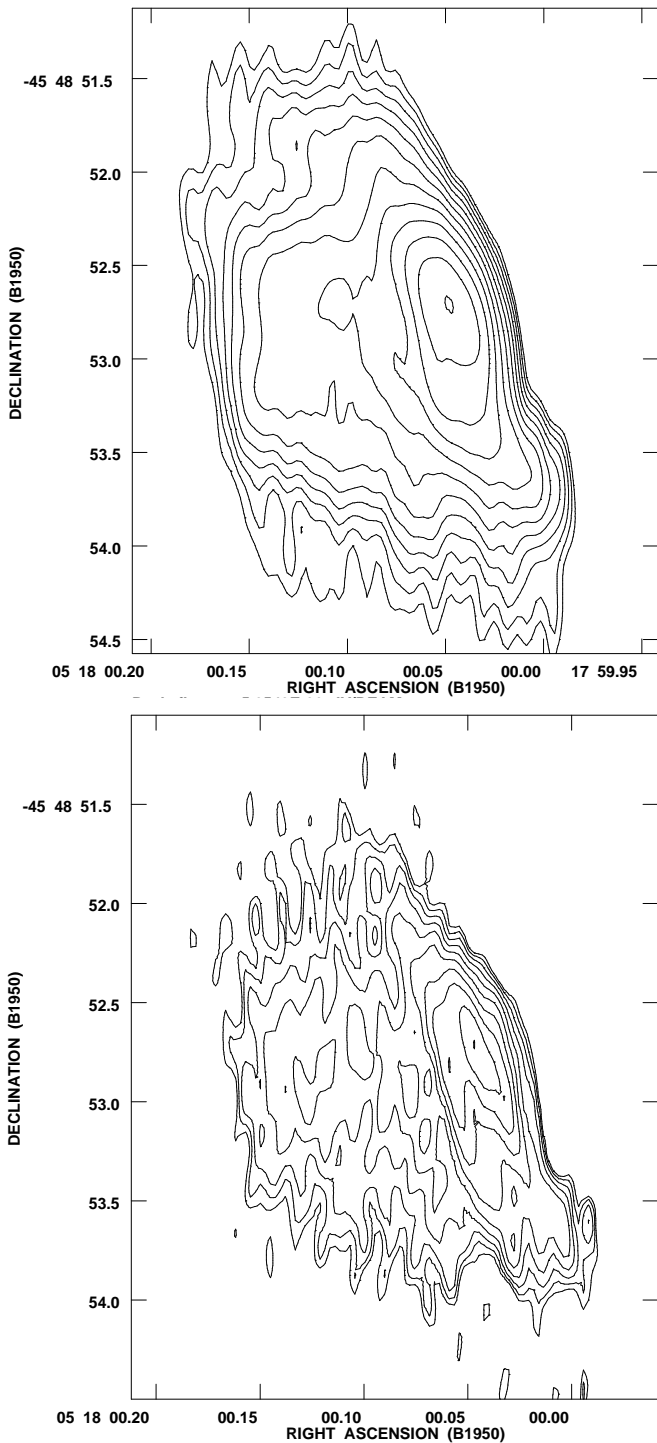
Fig. 19. Spectral steepening between $\lambda 2\,\mathrm{cm}$ and $\lambda 6\,\mathrm{cm}$ in the western hot spot region of Pictor A shown by a combined grey scale and contour plot. The grey scale shows α_2^6 at $2''5$ resolution over the range 0.7 to 1.3 superposed on the brightness contours at 2 cm wavelength and the same resolution. Contours are spaced by a factor of 2 between 0.552 and 70.71 % of the peak brightness of 878 mJy/beam.

Because of the very high brightness of the western hot spot, the possibility of synchrotron self absorption must be considered. Our observations at 73.8 MHz show no evidence of a flattening in the spectrum of the western hot spot. This result is not surprising, since the condition for unity optical depth from synchrotron self-absorption gives an expression for the necessary magnetic field in micro-Gauss: $B_{\mu G} \sim \nu_1^5 \theta^4 / 4 F_1^2$, where F_1 is the flux density in Jy at unity optical depth, ν_1 is the frequency in MHz of unity optical depth, and θ is the angular size in arcseconds. This shows that a magnetic field of 1 G would be required to give a noticeable absorption at 73 MHz. Using the equipartition magnetic field for the hot spot results in a predicted turnover of $\sim$ 1MHz – well below the observable window for ground-based observations.

Polarization Fig. 20 shows the polarization structure at $\lambda 3.6\,\mathrm{cm}$ with $4''5$ resolution (left), and $0''8 \times 0''2$ resolution (right). Both images show the significant polarization of the hot spot and filaments, with the projected magnetic fields lying in the usual way long the lines of constant brightness. The low-resolution figure also shows a region of polarized emission lying just to the east of the filament. The fields here are accurately aligned along the jet axis, indicating that this perhaps represents the jet, barely visible in total intensity. A similar fea-

Fig. 18. Pictor A's western hot spot proper at our highest resolution at 2 cm wavelength. We believe these images show hot spot structure at the highest physical resolution yet attained on any hot spot. The upper part shows the result of conventional CLEAN deconvolution, with a resolution of $0''45 \times 0''09$. The contours are spaced by a factor of $\sqrt{2}$ between 2.21 and 70.71 % of the peak brightness of 58.8 mJy/beam. The bottom panel shows the result of deconvolving by the AIPS maximum entropy procedure VTESS. The contours are spaced with the same factor as above but between 4.42 and 70.71 % of the maximum brightness of 1.20 mJy/pixel. The pixel size is $0''025$.
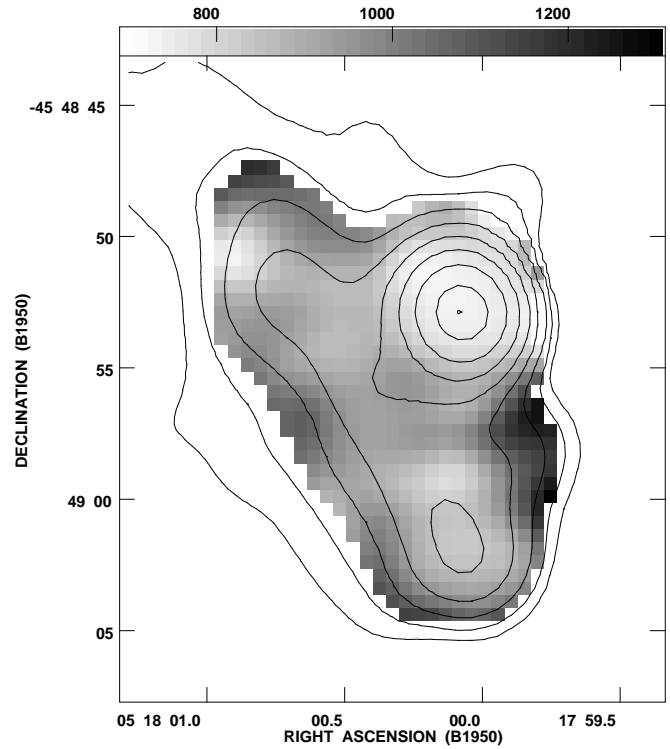
ture is seen at both $\lambda 6$ cm and $\lambda 2$ cm at the same resolution. The higher resolved figure displays the accurate alignment between the local intensity maxima and the apparent magnetic fields. Note how the fields accurately follow the bends in the filament, except in the far southern extension, where we presume line-of-sight effects have caused effective cancellation of the polarized emission.

Fig. 21 (left) shows the degree of polarization of the hot spot and its associated filament at $\lambda 3.6$ cm and $1''5$ resolution. The grey scale shows the degree of polarization, while the contours give the total intensity at the same band and resolution. The chief characteristic is the same as in the easternmost hot spot – the degree of polarization reaches the theoretical maximum at the outermost edges, and declines quickly to typically 20 % in the inner regions. This same pattern is repeated in the right panel of Fig. 21, showing the hot spot proper at $\lambda 2$ cm and $0''47$ by $0''09$ resolution.

5. Discussion

The very low brightness of the lobes leads to unusually low estimates of the magnetic field and confining medium. Following the usual assumptions about total minimum energy, we find that the equipartition magnetic field in the lobes to be $B_{eq} \sim 1\mu$G, the minimum pressure to be $P_{min} \sim 10^{-13}$dyn cm^{-2}, which if balanced by a thermal envelope with $T \sim 10^7$K requires $n_e \sim 7 \times 10^{-5}$cm^{-3}. The total energy in the lobes is about 7×10^{56} ergs.

The lobes exhibit considerable substructure as discussed in Sect. 4.1.1. The increased emissivity responsible for these structures may be due to projection effects in shell like structures. It could, however, also be due to increased magnetic field, increased particle density, or both. Since the emissivity of synchrotron radiation scales as $I_\nu \propto B^{1+\alpha} n_r x$, then the observed fractional brightness enhancement due to a 'filament' of length $x = fL$ (where L is the total lobe width) is roughly

$$\frac{\delta I}{I_0} = \frac{(1+\alpha)f\delta B}{B_0} + \frac{f\delta n_r}{n_{ro}}.$$

For Pictor A, the observed enhancement is $\sim 20\%$ from features with $f \sim 0.1$. Thus, B-field enhancements of roughly a factor of 5, or density enhancements of an order of magnitude are needed to explain the brightening. These enhancements will certainly overpressure these structures relative to the inter-filament regions, and suggest they must be dynamic features.

5.1. Spectral index of the lobes

Fig. 5 shows two interesting spectral effects in the emission from the lobes of Pictor A. The upper panel of the figure shows that the low frequency spectral index α_{20}^{90} is quite uniform throughout with a small but pronounced steepening in the central regions. In addition, there is a tendency for a slightly steeper spectral slope at the edges of the radio lobes. Flatter spectral slopes are noted near the hot spots – however the flat spectra in the

Table 3. Flux densities of the lobes of Pictor A

Frequency [MHz]	East Lobe [Jy]	West Lobe [Jy]	Ratio
74	237	213	1.11
327	86.3	94.3	0.92
1465	27.4	32.9	0.83
4995	8.77	12.0	0.73

vicinity of the western hot spot are very probably due to difficulties in deconvolution of the $\lambda 90$ cm image. These tendencies are greatly amplified in the high frequency spectral image α_6^{20} (lower panel of Fig. 5). Spectral indices exceeding 2.0 are observed at the edges of the source both in the central regions and along the periphery of the lobes. It is certain that even steeper – but not measurable – spectral slopes exist in these central regions, above and below the edges seen in the figures, since the $\lambda 6$ cm images are sensitivity limited. The curvature in these iso-slope lines (which are isochrones if the magnetic field is constant) is very striking – in particular, those in the western lobe are nearly circular, with a center only slightly displaced from the lobe center towards the western hot spot. This curvature is not unique to Pictor A – a similar effect, although not so pronounced, is observed in Cygnus A (Carilli et al. 1991).

The straightforward interpretation of the observed high-frequency steepening is that the lobe material near the galaxy and along the lobe periphery is older than that in the middle and near the hot spots. This general trend for the central regions is in accordance with the basic models for the evolution of luminous radio galaxies. However, the steepening along the edges is not in accord with a simple interpretation in which the back flow from the hot spots would be spread across the width of the lobes, so that the 'isochrones' would be expected to be straight lines, normal to the growth axis of the radio lobes. If the material near the periphery is indeed older, then it follows that interior regions of each lobe are filled with younger material, presumably supplied by the hot spots or the jet. This requires that there be a back flow of younger material, beginning with the hot spots and terminating along the lobe periphery and/or the central regions near the optical galaxy, or, originating from within the interior of the lobe, as would occur if the jets were 'leaky'.

However, this is not the only simple explanation. An alternative, suggested by Carilli et al.(1991), is that the material along the periphery is not older than that near the lobe centers, but has lost more energy, and thus appears older due to an enhanced magnetic field around the outskirts of the source. This interpretation removes the need to have the back flow operate preferentially along the source axis, but requires in its place a mechanism for enhanced field strengths along the periphery. However, this explanation requires a careful balancing of the magnetic fields and particle energy spectrum. An enhanced magnetic field along the lobe boundary would normally result in greatly increased emissivity – which is not observed. Thus, in the model, the particle energy spectrum must be sufficiently depleted to offset the required emissivity increase from the enhanced fields.
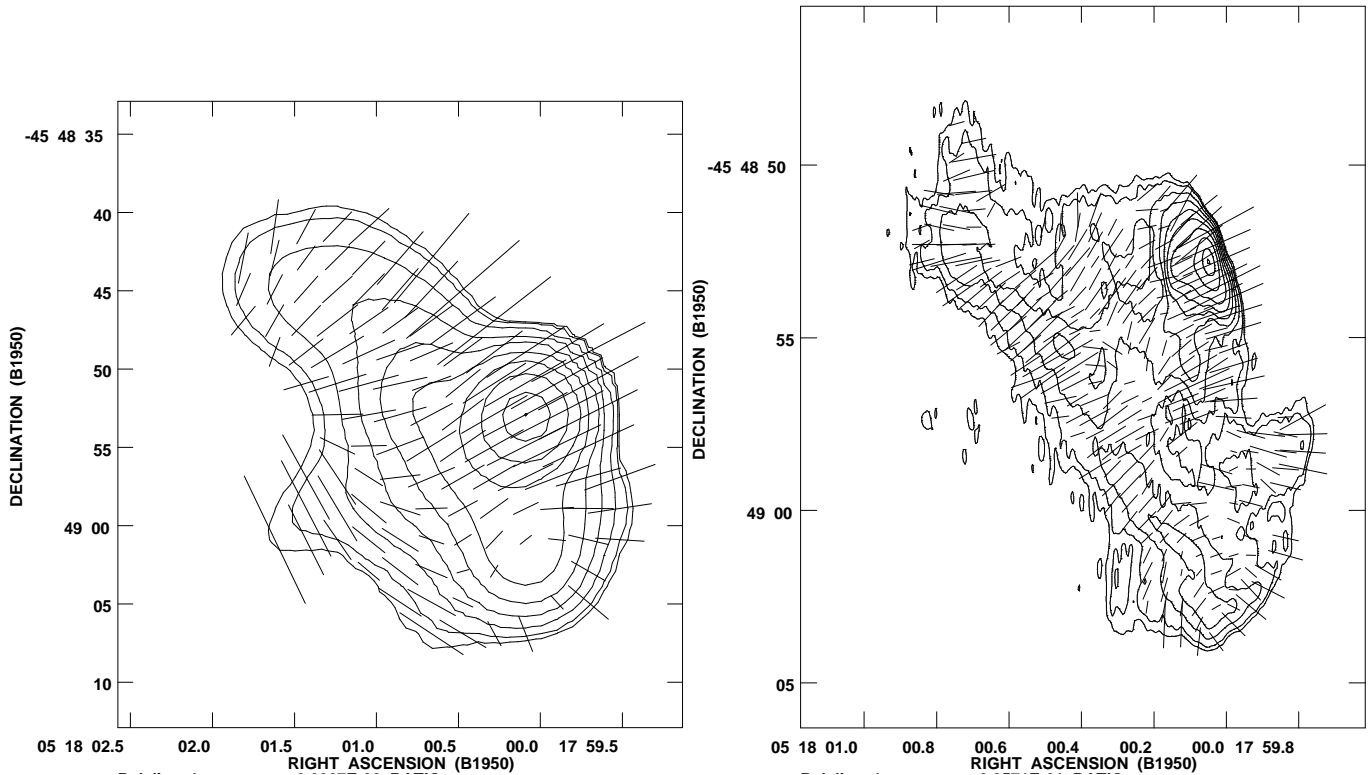
Fig. 20. Polarization of the western hot spot of Pictor A, at 3.6 cm wavelength with $4''$ resolution (left), and at $0.''77$ by $0.''17$ resolution (right). The lower resolution map shows the general features of this region, and is contoured at 0.391 % and then with a spacing of a factor of 2 between 0.552 and 70.71 % of the maximum intensity of 1.55 Jy/beam. The dashed lines again indicate the plane of the electric vector. Their lengths are proportional to the degree of polarization, with $1''$ equal to 6.67 %.
The higher resolution map at right is contoured the same way but here the peak brightness is 215 mJy/beam. The polarization is shown as in the left side, with a dash length of $1''$ equaling 28.6 % polarization.

We noted in Sect. 2.1 that total flux density measurements reveal the eastern lobe to have a steeper spectral index than the western lobe. This difference is seen in our detailed data. We show in Tab. 3 the summed flux densities of the lobes, and their ratio, at the four frequencies for which these measures can be made.

Note that these flux ratios are independent of our difficulties in establishing the flux density scale. A plot of these ratios *vs.* frequency gives an excellent fit to a powerlaw with slope 0.09, indicating that the eastern lobe has a spectral index steeper by this amount than the western lobe.

Fig. 5 (bottom) shows that the steepening effect is not localized to one particular region, but that nearly all regions of the eastern lobe have a steeper spectrum than the corresponding region in the western lobe (i.e., that portion of the western lobe located at the same distance from the nucleus and at the same position angle relative to the nucleus-hot spot axis). Given the pronounced steepening of the spectrum that occurs between $\lambda20$ cm and $\lambda6$ cm, it must be expected that the source will show a rather different appearance at $\lambda3.6$ cm. We plan on obtaining these data in the near future.

The spectral difference between the lobes in radio galaxies and quasars is not a new result – Liu and Pooley (1991b) re-

ported a strong correlation between depolarization and spectral slope in the sense that the lobe with greater depolarization also has the steeper spectral index. And so it is with Pictor A – the eastern lobe has a steeper spectral index, and displays less polarization at $\lambda20$ cm than the western lobe, while at $\lambda90$ cm it is completely depolarized. In a second paper (Liu and Pooley, 1991a), it is suggested that slight environmental differences can account for the correlation, so that the lobe in the denser environment will be smaller, and will display a greater spectral age due to increased magnetic fields brought on by the higher pressure. Examination of our images gives support to this idea. Both the length and width of the eastern lobe is smaller than that of the western. The ratio of lengths (core to hot spot) is 1.2, while the western lobe is about 5% wider. Assuming a depth equal to the observed width, the western lobe has a volume nearly 40% greater than the eastern. If each lobe contains equal total magnetic energy, the mean field in the eastern lobe will be 17% greater, leading to a break frequency 60% lower, assuming the two lobes have equal real ages and energies. The higher magnetic field of the eastern lobe will give an emissivity about $(B_e/B_w)^{\alpha+1} \sim 1.4$ times higher than the western lobe, which about cancels the volume difference, thus explaining the near equality of spectral flux densities. This argument assumes the
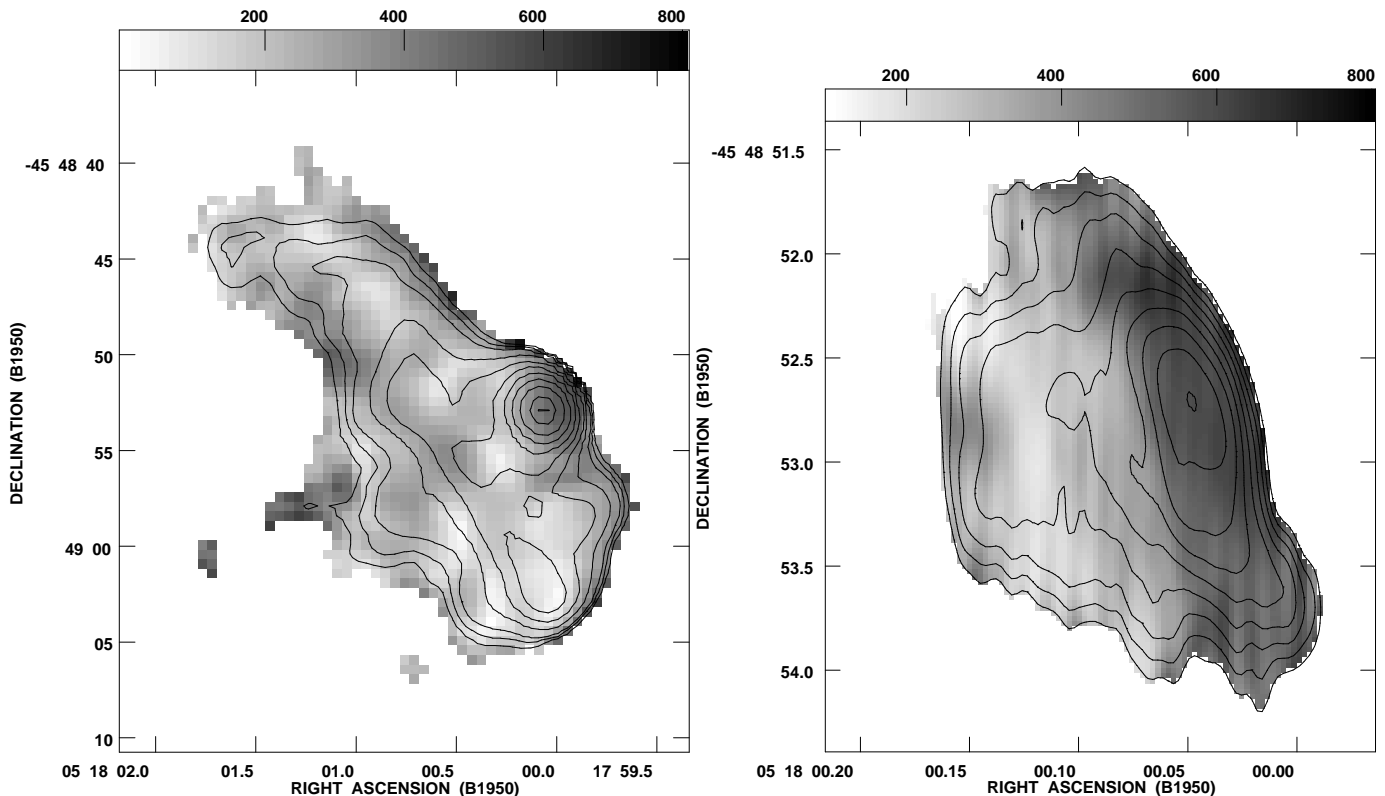
Fig. 21. Degree of polarization within the western hot spot of Pictor A. The grey scale displays the degree of polarization with a linear wedge extending from 0 to 80 % at left and 10 to 80 % at right; the contours show the total intensity. The $\lambda 3.6$ cm-map on the left side shows the region at $1\rlap{.}''5$ resolution, with contours between 0.28 and 70.71 % of the peak brightness of 940 mJy/beam, spaced by a factor of $\sqrt{2}$ til 0.552 %, then by a factor of 2. The filamentary plateau region is polarized at the 10 to 30 % level, while the leading edge of the hot spot shows polarization up to the theoretical maximum of about 70 %.
The map on the righthand side shows the hot spot itself at $\lambda 2$ cm at the highest resolution of $0\rlap{.}''47$ by $0\rlap{.}''09$. Contours are displayed at levels spaced a factor of $\sqrt{2}$ between 6.25 and 70.71 % the peak brightness of 57.5 mJy/beam.

total number of particles in each lobe is the same. This simple model cannot, however, explain the overall difference in spectral slope discussed in Sect. 2.1.

5.2. The western hot spot and its nearby filament

The outstanding single component of Pictor A is the western hot spot. The maximum surface brightness of the hot spot as revealed in the VTESS deconvolution shown in Fig. 18, is 2.05 Jy/$\square''$ – a brightness exceeded only by the hot spot of Cygnus A in a low redshift radio galaxy. The minimum pressure of this hot spot is $P_{\min} \sim 2 \times 10^{-9}$ dyn/cm^2 – about 1500 times that of the lobe. Assuming that the lobe is in pressure equilibrium with the galactic environment (an assumption we feel is well justified by the round and relaxed appearance of the lobes), and assuming that the hot spots are ram-pressure confined by expansion against the external medium, the hot spot Mach number is $M \sim \sqrt{P_{hs}/P_{lobe}} \sim 40$ – an extraordinarily high number required by the extraordinary brightness ratio between the hot spot and the lobes. The expansion velocity of the hot spot, $v_{exp} = M_{\mathrm{hs}} C_{\mathrm{s}}$ will be of order 0.1c to 0.3c, depending on the external gas temperature.

We noted in the introduction that one of our central goals was to investigate the radio structure corresponding to the optical emission discovered by Röser and Meisenheimer (1987). The correspondence is most directly shown in Figs. 22, which displays the $\lambda 3.6$ cm-image at $1\rlap{.}''5$ resolution together with the optical image at the same resolution. The close similarity is obvious. As shown by recent HST images (Thomson et al., 1995) this close match continues down to even much smaller scales. This gives strong weight to the interpretation that *all* of the optical emission is of synchrotron origin. This holds especially for the plateau or filament, which exhibits a steeper radio/optical spectrum of $\alpha = 0.98$ compared to the hot spot proper, whose $\alpha_{\mathrm{opt}}^{3.6}$ is 0.87. This spectrum is unusually steep when compared to other hot spots (Meisenheimer et al. (1997)), much steeper than predicted by the standard Fermi mechanism for particle acceleration.

Optical synchrotron radiation from the plateau region poses considerable problems for our understanding of how the relativistic particles giving rise to this emission, are accelerated. The plateau is $6.75/h$ kpc long, and is separated by typically $2.25/h$ kpc from the bright hot spot. The lifetime of electrons
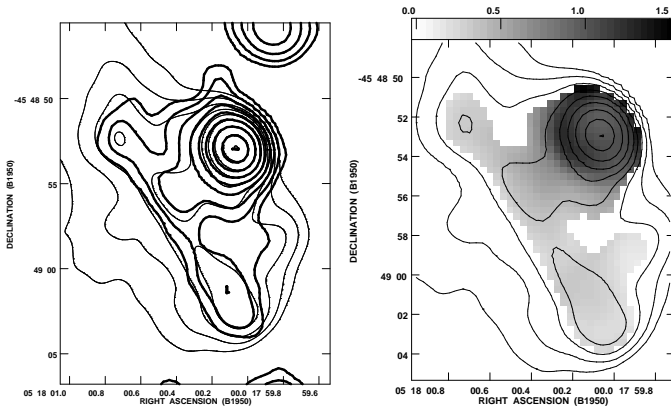
Fig. 22. A comparison of the radio and optical images of the western hot spot of Pictor A, at comparable resolutions of $1''.5$. The radio image is at 3.6 cm wavelength, the optical is a R-band image. In the **left** panel we show logarithmic isophotes for the radio (thin) and optical (thick lines) data (spacing factor 2). The feature extending to the north from the optical hot spot is a radio-quiet field object; a field galaxy also shows up towards the top end. The grey scale plot in the **right** panel shows the ratio optical over radio, normalized to 1 in the hot spot peak. The logarithmic isophotes give the total intensity at $\lambda 3.6$ cm for reference.

Fig. 23. The results of a simulation designed to determine whether the RM screen determined from our $10''$ data at $\lambda 20$ cm and $\lambda 6$ cm is sufficient to explain the observed complete depolarization of the eastern lobe. This image shows the predicted $\lambda 90$ cm polarized intensity from a simple model described in the text.

radiating at optical frequencies in fields typical of equipartition fields in the region is $\sim 10^3$ years – thus the observed optical emission from the filaments cannot be due to electrons provided from the hot spots. Fields low enough to permit direct streaming would increase the total energy by factors of more than 10^9, and can be rejected on energetics alone. We are thus led to conclude that the extended optical emission must be due to local acceleration and compression. We will discuss this problem in detail in a forthcoming paper, combining observations for this hot spot all across the electromagnetic spectrum from radio- to X-rays.

5.3. Depolarization

Fig. 11 shows that the eastern lobe of Pictor A is completely depolarized at 90 cm wavelength with $5''$ resolution. We also noted in Sect. 4.1.6 that the RM-screen in front of the eastern lobe is more complex, with a higher dispersion in the RM. This would appear to provide the means for low-frequency depolarization of this lobe, as the increased RM-dispersion will result in increased beam depolarization of the $\lambda 90$ cm radiation. To test this, we took our $\lambda 20$ cm polarized image, and constructed a predicted $\lambda 90$ cm image by rotating the observed $\lambda 20$ cm position angle by $\Delta\chi = RM(\lambda_{90}{}^2 - \lambda_{20}{}^2)$, with the RM image being formed from our $\lambda 20$ cm and $\lambda 6$ cm higher resolution data. The resulting images (in Stokes' Q and U) were then smoothed to the $\lambda 90$ cm resolution, and then converted to polarized flux and position angle for comparison to the observed maps.

The result, shown in Fig. 23, demonstrates that the simple external screen as revealed by the rotation measures is not sufficient to cause the total depolarization noted at $\lambda 90$ cm in the eastern lobe. Note in particular that the model predicts no depolarization of the eastern hot spots - this is simply a reflection
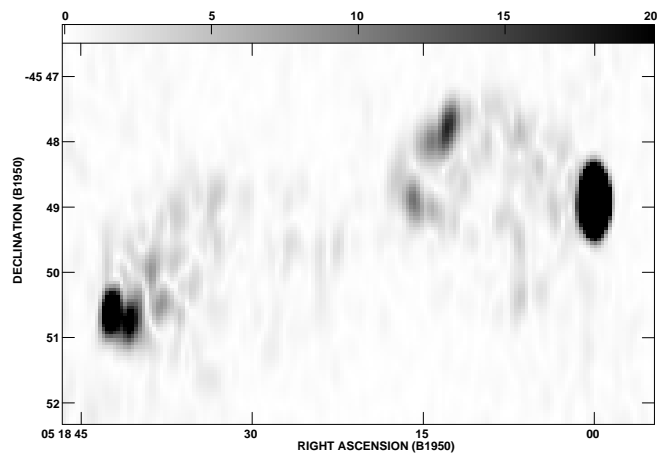
that the RM screen derived from the data has no gradients on such a small angular scale. Yet the $\lambda 90$ cm data clearly show the hot spots to have no measurable polarized signal.

The cause for the extra depolarization is unknown. Two possibilities are: (a) Part of the depolarization is internal to the source. Such a screen would not be completely removed by the RM analysis, or (b) small scale irregularities in the RM-screen unresolved in the current work, which cause higher rotation at $\lambda 90$ cm than predicted by the simple model considered. Arguing against the former mechanism are the observations of Dreher et al. (1987), Taylor and Perley (1993), and Perley and Taylor (1991) for Cygnus A, 3C 218, and 3C 295, all of which show pure λ^2-relations between the observed position angle and frequency, with much higher RMs than observed in this source. Further, recent ROSAT HRI images of Cygnus A (Carilli et al. (1994)) and Perseus A (Böhringer et al. (1993)) show clear evidence for a deficiency of X-ray emission along lines of sight passing through the radio lobes - clear evidence for an excavation of the X-ray emitting gas from these radio lobes. The processes responsible for excavating the lobes of those objects – all of which are located in dense X-ray cluster mediums – is presumably operating in Pictor A as well. It is difficult to imagine how this object could be entraining gas into the lobes, while other radio galaxies, in much denser mediums, do not. Suggestion (b), that the excess depolarization is due to unresolved small scale irregularities, is certainly possible – but cannot be tested without higher resolution observations at $\lambda 20$ cm or below – not possible until the VLA is expanded. A useful test would be to be able to calibrate the true position angles of the polarized emission at $\lambda 90$ cm – a future possibility with the sophisticated models of the ionosphere enabled by GPS receivers. However, it is not clear whether such models will be valid at such low elevations.

6. Conclusions

We have used the Very Large Array to map the prominent southern radio galaxy Pictor A at wavelengths from 400 cm through to 2 cm. The source comprises two diffuse circular lobes, and bright hot spots located near the extrema of the radio lobes. The radio lobes have a significantly different spectral index, with the eastern lobe having a spectral index greater by 0.09 than the western lobe. There are indications that this difference is common to all parts of the lobe, and is not due to accelerated ageing of the spectrum seen preferentially in one lobe. At $\lambda 6$ cm the distinctive signature of synchrotron ageing is seen around the periphery of the lobes and in the central regions near the radio nucleus. Both lobes demonstrate thick filamentary structure.

The lobes are polarized in the normal way, with circumferential magnetic fields seen on the lobe boundaries. The eastern lobe depolarizes at a shorter wavelength, and is completely depolarized at $\lambda 90$ cm, while the western lobe still maintains significant polarization at that wavelength. The mean rotation measure for both lobes is nearly identical, but the measured dispersion in the eastern lobe is much greater than that of the western lobe, leading to speculation that unresolved gradients in the eastern lobe are responsible for its greater depolarization at $\lambda 90$ cm and $\lambda 20$ cm. The eastern lobe is also the 'unjetted' lobe, and is thus likely to be directed away from our line of sight, and hence is likely viewed through a longer path length through the galactic atmosphere.

A weak jet is found, extending towards the western hot spot, but can be detected only about half way to the hot spot. No sign of the jet is seen on the sub-arcsecond scale. The jet/counter-jet ratio exceeds 3:1.

The eastern hot spot region comprises two distinct hot spots, each of which is completely resolved at a linear resolution of 1 kpc. The western hot spot is extremely bright, and extremely compact – maintaining structure down to a physical scale of $\sim$40 pc. It comprises two narrow, nearly parallel ridges oriented closely normal to the (likely) direction of the incoming radio jet. These fine-scale ridges are linearly polarized at $\sim$ 70%, the maximum possible with synchrotron radiation. Approximately 2 kpc from these bright ridges in the direction of the nucleus is a filamentary region oriented perpendicularly to the jet, and which is exactly coincident with the optical emission, thus giving very strong weight to the interpretation of the optical emission as synchrotron. With reference to other extragalactic radio sources with extended optical emission (M 87 (Neumann et al., 1995) and 3C 273 (Conway and Röser, 1993)) Pictor A provides further support that this extended optical synchrotron emission must arise from local acceleration and compression processes, although how this occurs is not simply explained by any current theory of radio sources.

References

Baars, J. W. M., Genzel, R., Pauliny-Toth, I. I. K., and Witzel, A.: 1977, A&A 61, 99

Berge, G. L. and Seielstad, G. A.: 1967, ApJ 148, 367

Black, A. R. S., Baum, S. A., Leahy, J. P., Perley, R. A., Riley, J. M., and Scheuer, P. A. G.: 1992, MNRAS 256, 186

Böhringer, H., Voges, W., Fabian, A. C., Edge, A. C., and Neumann, D. M.: 1993, MNRAS 264, L25

Bolton, J. G., Gardner, F. F., and Mackey, M. B.: 1964, Aust. J. Phys. 17, 340

Bolton, J. G., Stanley, G. J., and Slee, O. B.: 1954, Austral. J. Sci. Res. 7, 110

Broten, N. W., Cooper, B. F. C., Gardner, F. F., Minette, H. C., Price, R. M., Tonking, F. G., and Tabsley, D. E.: 1965, Aust. J. Phys. 18, 85

Carilli, C. L., Perley, R. A., and Harris, D. H.: 1994, MNRAS 270, 173

Carilli, C. L., Perley, R. A., Leahy, J. L., and Dreher, J. W.: 1991, ApJ 383, 554

Christiansen, W. N., Frater, R. H., Watkinson, A., O'Sullivan, J. D., Lockhart, J. A., and Goss, W. M.: 1977, MNRAS 181, 183

Clarke, D. A., Bridle, A. H., Burns, J. O., Perley, R. A., and Norman, M. L.: 1992, ApJ 385, 173

Conway, R. G. and Röser, H.-J.: 1993, in H.-J. Röser and K. Meisenheimer (eds.), Jets in Extragalactic Radio Sources, No. 421 in Lecture Notes in Physics, pp 199-216, Springer Verlag, Berlin Heidelberg New York

Danziger, I. J., Fosbury, R. A. E., and Penston, M. V.: 1974, MNRAS 179, 41P

Davies, R. D. and Gardner, F. F.: 1970, Aust. J. Phys. 23, 59

Dreher, J. W., Carilli, C. L., and Perley, R. A.: 1987, ApJ 316, 611

Dreher, J. W. and Feigelson, E. D.: 1984, Nat 308, 43

Ebnetter, K. A., van Breugel, W. J. M., Fomalont, E. B., and Ekers, R.: 1989, ApJ 346, L17

Ekers, R. D.: 1967, Ph.D. thesis, Australia National University, Canberra

Ekers, R. D.: 1969, Austr. J. Phys. Astrophys. Suppl. 6, 1

Fanaroff, B. L. and Riley, J. M.: 1974, MNRAS 167, 31P

Fomalont, E. B.: 1989, in (Perley et al., 1989), p. 213

Fomalont, E. B., Ebnetter, K. A., and van Breugel, W. J. M.: 1989, ApJ 346, L17

Gardner, F. F. and Whiteoak, J. B.: 1971, Aust. J. Phys. 24, 1971

Gardner, F. F., Whiteoak, J. B., and Morris, D.: 1975, Aust. J. Phys. Astrophys. Suppl. 35, 1

Garrington, S. T. and Conway, R. G.: 1991, MNRAS 250, 198

Garrington, S. T., Leahy, J. P., Conway, R. G., and Laing, R. A.: 1989, Nat 331, 147

Haves, P.: 1975, MNRAS 173, 553

Hines, D. C., Owen, F. N., and Eilek, J. A.: 1989, ApJ 347, 713

Laing, R. A.: 1988, Nat 331, 149

Laing, R. A.: 1989, in (Meisenheimer and Röser, 1989), p. 27

Leahy, J. P. and Perley, R. A.: 1991, AJ 102, 537

Leahy, J. P. and Williams, A. G.: 1984, MNRAS 225, 1

Liu, R. and Pooley, G.: 1991a, MNRAS 253, 669

Liu, R. and Pooley, G.: 1991b, MNRAS 249, 343

Maltby, P. and Moffet, A. T.: 1962, ApJS 7, 141

Meisenheimer, K. and Röser, H.-J. (eds.): 1989, Hot Spots in Extragalactic Radio Sources, No. 327 in Lecture Notes in Physics, Berlin Heidelberg New York, Springer Verlag

Meisenheimer, K., Yates, M. G., and Röser, H.-J.: 1997, A&A ?, ?, (accepted)

Mills, B. Y.: 1952, Austral. J. Sci. Res. A5, 266

Mills, B. Y., Slee, O. B., and Hill, E. R.: 1960, Aust. J. Phys. 13, 676

Morimoto, M. and Lockhart, I. A.: 1968, Proc. Astron. Soc. Aust. 1, 99

Neumann, M., Meisenheimer, K., Röser, H.-J., and Stickel, M.: 1995, A&A 296, 662

Perley, R. A., Dreher, J. W., and Cowan, J. J.: 1984, ApJ 285, L35

Perley, R. A., Schwab, F. R., and Bridle, A. H. (eds.): 1989, Synthesis Imaging in Radio Astronomy, Vol. 6 of Astronomical Society of the Pacific Conference Proceedings, San Francisco, Astronomical Society of the Pacific, Astronomical Society of the Pacific

Perley, R. A. and Taylor, G. B.: 1991, AJ 101, 1623

Prestage, R. M.: 1985, Ph.D. thesis, University of Edinburgh

Robertson, J. G.: 1973, Aust. J. Phys. 26, 403

Röser, H.-J.: 1989, in (Meisenheimer and Röser, 1989), pp 91-114

Röser, H.-J. and Meisenheimer, K.: 1987, ApJ 314, 70

Schilizzi, R. T.: 1976, AJ 81, 946

Schilizzi, R. T. and McAdam, W. B.: 1975, Mem. R. Astron. Soc. 79, 1

Schmidt, M.: 1965, ApJ 141, 1

Schwarz, U. J., Whiteoak, J. B., and Cole, D. J.: 1971, Aust. J. Phys. 27, 563

Seielstad, G. A.: 1967, ApJ 147, 24

Seielstad, G. A. and Weiler, K. W.: 1969, Aust. J. Phys. 158, 85

Slee, O. B. and Sheridan, K. V.: 1975, Proc. Astron. Soc. Aust. 2, 0

Stanley, G. J. and Slee, O. B.: 1950, Austral. J. Sci. Res. A3, 234

Taylor, G. B.: 1991, Ph.D. thesis, U.C.L.A.

Taylor, G. B. and Perley, R. A.: 1993, ApJ 416, 554

Thomson, R. C., Crane, P., and Mackay, C. D.: 1995, ApJ 446, L93

van Breugel, W. J. M. and Fomalont, E.: 1984, ApJ 282, L55

Westerlund, B. E. and Wall, J. V.: 1969, AJ 74, 335

Wills, B. J.: 1975, Aust. J. Phys. Astrophys. Suppl. 38, 1

Zukowski, E. L.: 1990, Ph.D. thesis, University of Toronto